Danish Climate Centre

DMI, Ministry of Transport

The climate of the 21st century: Transient simulations with a coupled atmosphere-ocean general circulation model

Revised version

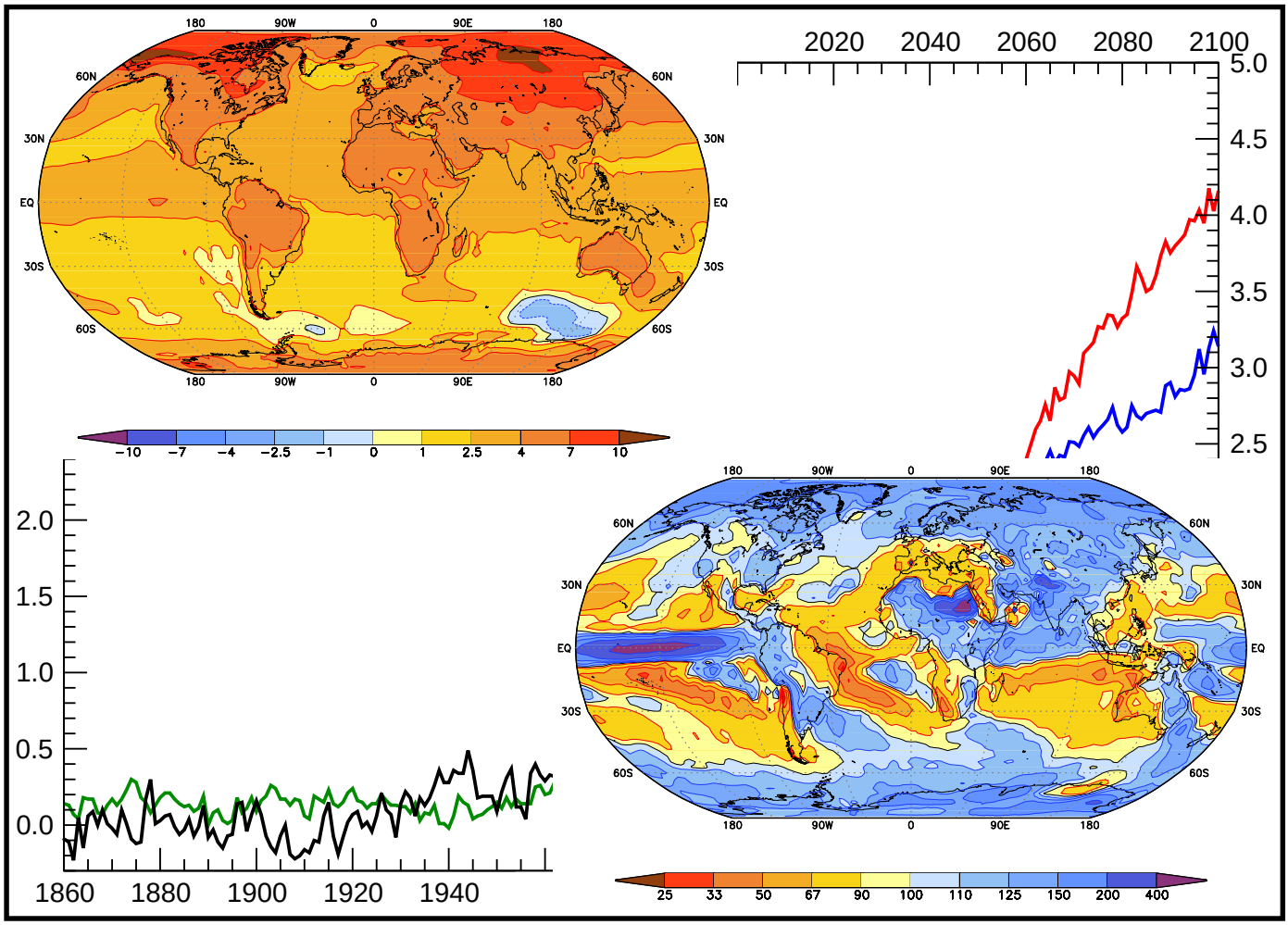

Martin Stendel **Torben Schmith**

Danish Meteorological Institute and Danish Climate Centre

Erich Roeckner **Ulrich Cubasch**

Max-Planck-Institut für Meteorologie ***Freie Universität Berlin***

Report 02-1

The climate of the 21st century: Transient simulations with a coupled atmosphere-ocean general circulation model. Revised version

Martin Stendel, Torben Schmith, Erich Roeckner and Ulrich Cubasch

ISBN: 87-7478-464-1 (original ISBN was 87-7478-427-7)
ISSN: 1398-490-X (printed)
ISSN: 1399-1957 (online)

Danish Meteorological Institute
Lyngbyvej 100
DK-2100 Copenhagen Ø
Denmark

Phone: +45 3915 7500
Fax: +45 3915 1080

www.dmi.dk

Abstract

The coupled atmosphere-ocean general circulation model ECHAM4-OPYC3 is used to assess the time-dependent climate response to changing concentrations of greenhouse gases and sulfate aerosol. For the period 1860 to 1990, the concentrations have been prescribed according to observations. For the period 1990 to 2100, projections according to the International Panel on Climate Change (IPCC) scenarios A2 and B2 have been used. The tropospheric sulfur cycle is calculated from past observations and future projections of sulfur emissions according to these scenarios. Both the direct and the indirect (cloud albedo) radiative effect of the aerosols are considered. The climate response is comparable to other simulations that include aerosol effects, i.e. the warming is reduced by the aerosols. However, it is larger than in experiments using the IS92a scenario, in particular in the second half of the 21st century, when sulfur emissions decrease in both scenarios, so that the direct aerosol effect can be outweighed by the increase in absorbed shortwave radiation. An increase of precipitation over land and a concomitant decrease over the oceans is found. Sea ice decreases dramatically in the shelf seas of the Arctic, whereas there are only minor changes for the Antarctic sea ice. A poleward displacement and intensification of the storm tracks is found in both hemispheres.

1. Introduction

A comprehensive description of the components of the climate system (atmosphere, ocean, cryosphere, land surface) and their mutual interactions is crucial for understanding Earth's climate under the influence of various natural and human factors, such as time-varying atmospheric concentrations of greenhouse gases and sulfate aerosols. Coupled models of the atmosphere and ocean (AOGCMs) are suitable tools for understanding the past, present and future climate.

Due to the vast differences in typical time scales, which are on the order of one week for the atmosphere, a couple of months for the ocean mixed layer and the land surface and up to millennia for the deep ocean, simulations of the coupled system require restrictions in complexity and resolution.

It is well established from chemical transport models that sulfate aerosols exert a cooling effect on the atmosphere (see e.g. the reviews by Shine and Forster, 1999 and Haywood and Boucher, 2000). Estimates for the global mean radiative forcing due to the direct aerosol effect (i.e., due to aerosol scattering and the absorption of solar and infrared radiation) range from -0.26 Wm^{-2}

(Graf et al., 1997) to -0.82 Wm^{-2} (Haywood and Ramaswamy, 1998). The size of the indirect effect (i.e., alteration of the microphysical properties of clouds) is very uncertain. It is estimated between -0.3 Wm^{-2} and -1.8 Wm^{-2} for changes in droplet concentration and size (e.g. Jones and Slingo, 1996; Chuang et al., 2000) and between 0 and -2 Wm^{-2} for changes in precipitation efficiency and cloud lifetime and thickness (e.g. Jones et al., 1999; Rotstayn, 1999). The radiative effects of aerosols may therefore be of comparable magnitude (but opposite sign) to the radiative forcing of the well-mixed greenhouse gases, CO_2, CH_4, N_2O and halocarbons, which are presently estimated at slightly less than 2.5 Wm^{-2} (e.g. Hansen et al., 1997a,b).

Despite the importance of both the direct and indirect aerosol effect, the sulfur cycle has been treated in a rather simplistic way until recently. These simplifications include the prescription of off-line calculated sulfate burdens, a rather crude parameterization of the direct effect as a perturbation of surface albedo and the neglection of the indirect radiative effect. There are also a number of mainly or entirely anthropogenic sources of aerosols that exert radiative forcing. However, these have not been accounted for in this study, either because these forcings are rather small, as for black and organic carbon aerosol from fossil fuel combustion (Penner et al., 1998; Grant et al. 1999; Cooke et al., 1999), or they are very uncertain, partly even in sign, as for aerosols from mineral dust, biomass burning and nitrate (e.g. Miller and Tegen, 1998; Jacobson, 2000a,b; Adams et al., 2000).

In this study, we use the coupled atmosphere-ocean model ECHAM4/OPYC3 which has been described by Roeckner et al. (1999). It includes a model of the tropospheric sulfur cycle (Feichter et al., 1996, 1997), which is driven by prescribed surface emissions. Both the direct and the first indirect aerosol effect (effect of aerosols on droplet concentration and size) are taken into account, and the respective model estimates (Roeckner et al., 1999) are within the range of uncertainties discussed earlier. The effect on cloud lifetime is neglected. The AOGCM includes the effect of prescribed changes in tropospheric ozone, whereas the forcing due to stratospheric ozone depletion (Ramaswamy et al., 1996) is also neglected.

Two time-dependent forcing experiments according to the new IPCC SRES scenarios with prescribed concentrations of greenhouse gases and halocarbons and emissions of sulfur have been conducted for the period 1990-2100. These scenarios have been developed and published by IPCC (Nakicenovic et al, 2000) to replace its earlier IS92 scenarios. These new scenarios are based on a review of the literature, the development of "storylines", and the quantification of

these storylines with the help of six different integrated models from different countries. Compared to the older IS92 scenarios, which were based on the economical data before the fall of the Iron Curtain, the current scenarios introduce many innovative aspects, such as a narrative description of the scenarios, inclusion of information on the availability of energy technologies, and an analysis of international equity issues.

Out of the 40 SRES scenarios, four marker scenarios have been selected, which are representative for a whole family of scenarios:

- A1 assumes a global cooperation and a rapid adaptation of new technologies, together with a stabilization of the population;
- A2 assumes a regionally limited cooperation and a slower adaptation of new technologies, together with an unstabilized population growth;
- B1 assumes a global ecological development, together with a stabilization of the population;
- B2 anticipates a regionally limited ecological development.

All these scenarios define a range of sulfur emissions smaller than the IS92 range (compare Fig. 1). The B scenarios have a lower CO_2 emission than IS92a, while A2 assumes higher emissions. A1 anticipates a stabilization during the middle of the next century. From these four marker scenarios, A2 and B2 have been selected for this study because they seem to be most realistic.

This report is intended as a reference to the results of the SRES simulations that have been performed in cooperation between the Danish Meteorological Institute (DMI) in Copenhagen and the Max Planck Institute for Meteorology (MPI) in Hamburg. The focus is on changes (both in the atmosphere and the ocean) compared to present-day climate, as simulated by the model. A comparison of these model-simulated data with observations has been done by Bengtsson et al. (1999). In section 2, the components of the model (atmosphere, ocean, sulfur cycle) are briefly described, and section 3 explains the experimental design. Details of the sulfur simulation are given in section 4. The atmospheric and oceanic response are dealt with in sections 5 and 6, respectively. A discussion and summary conclude the paper in section 7.

This report is a revised version of Danish Climate Centre Report 00-6 (2000). The revision became necessary because the model runs described in that report suffered from an error in the model setup that caused unrealistic fluxes of several quantities in the tropical Atlantic.

2. Model description

The AOGCM that is used for this study consists of an atmospheric and an oceanic component. The atmospheric model ECHAM4 is described in detail in Roeckner et al. (1996). A 19-level hybrid sigma-pressure coordinate system is used. The vertical domain extends up to the pressure level of 10 hPa. Prognostic variables are vorticity, divergence, the logarithm of surface pressure, temperature, specific humidity and mixing ratio of total cloud water. Except for the water components the prognostic variables are represented by spherical harmonics with triangular truncation at wavenumber 42 (T42). A semi-implicit time stepping scheme is used together with a weak time filter. The time step for dynamics and physics is 24 min, and the radiation time step is 2 hours. Both seasonal and diurnal cycles in solar forcing are simulated.

For the transport of water vapor, cloud water and chemical constituents a semi-Lagrangian scheme is used (Williamson and Rasch, 1994). Horizontal diffusion is expressed in the form of a hyper-Laplacian which essentially confines the damping to the high-wavenumber end of the spectrum. Turbulent surface fluxes are calculated from Monin-Obukhov similarity theory (Louis, 1979). Within and above the atmospheric boundary layer, a higher-order closure scheme is used to compute the turbulent transfer of momentum, heat, moisture, cloud water and sulfate aerosol. Drag associated with orographic gravity waves is simulated after Miller et al. (1989), using directionally dependent subgrid-scale orographic variances. The soil model comprises the budgets of heat and water in the soil, the snow pack over land and the heat budget of land ice. Vegetation effects such as the interception of rain and snow in the canopy and the stomatal control of evapotranspiration are parameterized in an idealized way. The local runoff scheme is based on catchment considerations and takes into account subgrid-scale variations of field capacity over inhomogeneous terrain. Land surface parameters such as background albedo, roughness length, vegetation type, leaf area index and soil parameters like water holding capacity, heat capacity and thermal conductivity follow Claussen et al. (1994).

Based on Tiedtke (1989) and modifications by Nordeng (1994), the parameterization of cumulus convection is parameterized according to a bulk mass flux concept. Organized entrainment is related to buoyancy, organized detrainment is computed for a spectrum of clouds detraining at different heights, and an adjustment-type closure is used for deep cumulus convection (instead of the moisture convergence closure applied in the Tiedtke scheme). The stratiform cloud water content is calculated from the respective budget equation including sources and sinks due to phase changes and precipitation formation by coalescence of cloud droplets and gravitational

settling of ice crystals (Roeckner, 1995). The convective cloud water detrained at the top of cumulus clouds is used as a source term in the stratiform cloud water equation. Fractional cloud cover is parameterized in terms of relative humidity.

The transfer of solar radiation has been parameterized according to Fouquart and Bonnel (1980), while the parameterization of longwave radiation follows Morcrette et al. (1986) with a few modifications like the consideration of additional greenhouse gases (methane, nitrous oxide and 16 CFCs, HCFCs and HFCs) and the 14.6 μm band of ozone. Moreover, the water vapor continuum has been revised to include temperature weighted band averages of e-type absorption and also a band dependent ratio of (*p*-*e*)-type to *e*-type continuum absorption (Giorgetta and Wild, 1995). The single scattering properties of cloud droplets and ice crystals are derived from Mie theory with suitable adaptation to the broad-band model (Rockel et al., 1991), and the effective radius of droplets and ice crystals is parameterized in terms of the liquid and ice water content, respectively (Roeckner, 1995).

The model version used here calculates basic aspects of the tropospheric sulfur cycle, such as transport and deposition, and partly also the chemistry (Feichter et al., 1996, 1997). Dimethylsulfide (DMS), gaseous sulfur dioxide (SO_2) and sulfate aerosol (SO_4^{2-}) are used as prognostic variables. It is important to note that biogenic emission from oceans, soils and plants are assumed to occur as DMS, while noneruptive volcanic emissions, the burning of biomass and the combustion of fossil fuels are assumed to take place as SO_2. Transport and diffusion of the sulfur species are treated as for water vapor. A deposition velocity, dependent on the species and on the state of the surface, is used to calculate dry deposition. Wet deposition is parameterized by means of the local precipitation formation rate. During daytime, DMS and SO_2 are oxidized by hydroxyl radicals (OH^-), whereas during the night DMS reacts with nitrate radicals (NO_3^-). In the aqueous phase, SO_2 is oxidized by ozone (O_3) and hydrogen peroxide (H_2O_2). These species are not calculated in ECHAM4, but rather prescribed as monthly-mean three-dimensional fields, according to estimates by a chemistry model coupled to ECHAM4 (Roelofs and Lelieveld, 1995). In any case, the final product of the oxidation of SO_2 is sulfate aerosol, which interacts radiatively with the atmospheric model through direct and indirect effects. These are discussed in section 3.

The ocean model is an extended version (level 3) of the OPYC model (Oberhuber, 1993) and consists of three submodels. In the submodel for the interior ocean, equations for momentum, mass, heat and salt are solved in isopycnal coordinates. Horizontal mixing of momentum is considered as a function of the local Rossby deformation radius, whereas horizontal diffusion for temperature and salinity is dependent on the deformation of the flow. Vertical mixing is calculated with an entrainment/detrainment approach. A standard convection scheme is used, which removes vertical instabilities instantaneously. The submodel for the surface mixed layer is coupled to the deep ocean through budget equations for turbulent kinetic and mean potential energy. The third component is a sea-ice model that calculates ice momentum, ice and snow thickness and ice concentration. Viscous-plastic rheology is used. The ocean model has 11 layers. The horizontal resolution is identical to that of the atmosphere (~2.8°, which is equivalent to the atmospheric T42 Gaussian grid) poleward of 36°. For lower latitudes, the meridional grid spacing is gradually decreased to 0.5° at the equator.

The model components are quasi-synchronously coupled and exchange information once daily. Daily-averaged surface fluxes of momentum, heat and fresh water are given by the atmospheric model, whereas the ocean model calculates daily averages of the sea surface temperature (SST) and of the ice variables. The model employs annual mean flux corrections for heat and freshwater.

3. Experimental design

Two 110 year experiments with time-dependent forcing have been performed. These are compared to a 300 year unforced control simulation and to present-day climate, expressed as the average over the period 1961-1990. Both simulations are described in Roeckner et al. (1999). The transient runs have been set up as follows. Concentrations of well-mixed greenhouse gases (CO_2, CH_4 and N_2O and halocarbons[1]) are prescribed as a function of time. For the period 1860 to 1990, the concentrations are derived from observations. For the period 1990 to 2100, the concentrations of these gases are prescribed according to the SRES marker scenarios A2 and B2, respectively. These scenarios are described in detail in Nakicenovic et al. (2000).

[1] This includes chlorofluorocarbons (CFC-11, -12, -113, -114, -115), hydrochlorofluorocarbons (HCFC-22, -123, -141b), hydrofluorocarbons (HFC-125, -134a -152a), carbon tetrachloride (CCl_4) and methylchloroform (CH_3CCl_3).

As discussed in Roeckner et al. (1999), present-day observations have been used to estimate the flux correction and the spinup of the ocean (Bacher et al., 1998), and present-day concentrations of the greenhouse gases have been applied in the control run. This implies that the control simulation is not depicting preindustrial, but present-day conditions. Therefore, there is a warm bias in the initial state, but this bias is carried through the whole simulation, so that the derived trends are not affected.

In addition to well-mixed greenhouse gases and halogenated carbohydrates, the tropospheric sulfur cycle is also simulated. Only anthropogenic sources are taken into account, but the biogenic and volcanic sulfur emissions are neglected (see Roeckner et al., 1999). For the period 1990 to 2100, the emissions are given every ten years (Nakicenovic et al., 2000), with linear interpolation in between. Both the direct radiative effect and the indirect effect on cloud albedo are taken into account, as discussed in detail in Roeckner et al. (1999). Furthermore, the tropospheric ozone distribution is dependent on the concentration of the precursor gases O_3, H_2O_2, OH^- and NO_3^-. These concentrations are available for 1860, 1985 and 2050. Intermediate values are obtained by linear interpolation, whereas after 2050 the concentrations have been held constant at the 2050 value.

4. Sulfur emissions and radiative forcing

Fig. 1 shows radiative forcings and sulfur emissions for scenarios and observations according to Hansen et al. (2000). Until 2100, the total forcing of all greenhouse gases rises from the 1990 value of 2.0 Wm^{-2} to 8.1 Wm^{-2} for scenario A2 and 5.5 Wm^{-2} for scenario B2. The greenhouse gas concentrations in the old IS92a scenario are very similar to A2.

Larger differences between the scenarios are found for the sulfur emissions. Globally, the emissions in scenario A2 are expected to increase by 50% until the 2030s and then decrease gradually, so that the 2100 emissions are approximately as large as present-day emissions. In scenario B2, a gradual decrease is assumed with the emissions in 2100 approximately 30% less than today. Compared to IS92a, the emissions in 2050 are reduced to about 70% in A2 and 40% in B2.

In Fig. 2, the geographical distributions of sulfur emissions for both A2 and B2 scenarios are given for selected years. While for present-day conditions most of the emissions come from North America and Europe, the largest emittents by 2030 will be China, India and South Africa. In the second half of the century, a decrease of emissions is assumed everywhere.

5. Atmospheric climate response

5.1 Temperature and sea ice cover

Fig. 3 shows the temporal evolution of the global mean temperature with respect to the control run. To depict the general trend, all values have been smoothed by a 5-year running mean. For global values, the trends generally follow the radiative forcing. The increase of the global average temperature of about 2-3 K during the 21st century is consistent with previous studies (e.g. IPCC, 1996; Hegerl et al., 1997; Mitchell and Johns, 1997). The aerosol effect on global temperature is clearly evident in Fig. 3. Although the greenhouse gas forcing in A2 proceeds faster than in B2, the warming, until about 2050, is actually smaller. This is due to both enhanced sulfur emissions during the first phase of the simulation (cf. Fig. 1) and internal variability which causes the "plateau" in global mean temperature between about 2010 and 2040. For the first (1990-2019), middle (2030-2059) and last thirty years of the simulation (2070-2099), the decadal trends in scenario A2 (B2) are 0.27 (0.23), 0.39 (0.30) and 0.38 (0.20) K/decade, respectively.

The geographical pattern of temperature change, expressed as the difference between the last three decades (2071-2100) and the period 1961-1990 of the transient simulations is shown in Fig. 4. In boreal winter (DJF), both scenarios show maximum warming of up to 11 K in the Canadian and Siberian Arctic. In agreement with many previous studies (summarized e.g. in Kattenberg et al., 1996), the warming over land is larger than that over the oceans and exceeds 2.5 K almost everywhere in the Northern Hemisphere. In the Southern Hemisphere, warming of up to 4 K is simulated. Regional differences are smaller than in the Northern Hemisphere. In JJA, the warming is generally more uniform than in DJF. Maximum warming exceeding 6 K is found over Greenland as well as the subtropical regions Asia, North America and Europe. Over the oceans, we find considerably smaller warming (generally 2.5-4 K in the Northern and less than 2 K in the Southern Hemisphere). Regions with strong vertical mixing, such as the Southern Ocean, even exhibit a temperature decrease independent of season in both scenarios.

In good agreement with other studies (see discussion in Kattenberg et al., 1996), we find a general decrease of the diurnal temperature range (Fig. 5). This is caused by the increased water vapor content of the atmosphere (approximately 30%; not shown) that leads to a reduced longwave emission during nighttime, whereas, due to stronger clear-sky absorption during daytime (see Table 2), less solar radiation reaches the surface (compare Stenchikov and Robock, 1995).

On a regional scale, other factors are also important, such as changes in snow extent and precipitation (Canadian and Siberian Arctic in DJF, compare Fig. 6), soil moisture (Brazil throughout the year, India, Europe, Sahel in JJA, Fig. 7) and cloud cover (Brazil throughout the year, East Asia in JJA, Fig. 8). The increase of water vapor content leads also to an increase in dew point (not shown) which implies considerably less comfortable living conditions in some heavily populated low latitude regions, in particular India and Southeast Asia.

The warming of the globe goes along with a melting of sea ice, in particular in the Arctic. From Fig. 9, which shows the temporal evolution of the Arctic ice cover, it can be seen that the reduction in sea ice cover is approximately 40%, with a particularly strong retreat in summer. Not only the sea ice extent, but also the thickness of the ice decreases. Fig. 10 shows the changes in Arctic sea ice volume for the period 2071-2100 minus 1961-1990. It can be seen that this quantity decreases by nearly two thirds in winter and about three quarters in summer. This has strong effects on the shelf seas, in particular the Barents Sea, where, according to scenario A2, sea ice vanishes almost completely (Fig. 11). Sea ice change is much smaller around Antarctica (not shown), and there is considerable interdecadal variability of sea ice cover exceeding the climate change signal. This variability is also present in the uncoupled ocean model (Oberhuber, pers. comm.).

5.2 Hydrological cycle

The components of the water budget are given in Table 1. In contrast to the findings of Roeckner et al. (1999), the global hydrological cycle is slightly enhanced. Over the oceans, we find approximately a 1% increase in evaporation and a 1% decrease in precipitation with respect to the control run, so that there is an excess of water than can be precipitated over land, where consequently we find an enhancement of the hydrological cycle.

Globally, the change in precipitation for the last 30 years of both scenarios with respect to 1961-1990 is quite small in both scenarios (2%). There are, however, distinct regional differences (Fig. 6). Winter precipitation generally increases in the temperate latitudes by typically 10-30%, but doubles in East Siberia. In JJA, we find a general decrease of precipitation over large parts of the subtropics and midlatitudes of both hemispheres, in good agreement with other models (see also Machenhauer et al., 1998 and May, 1999). With the exception of the Sahel, where summer precipitation increases slightly, a decrease of precipitation in the subtropics is simulated throughout the year. This mainly affects the oceans, but also some land areas that are threat-

Table 1: 300 year mean water fluxes in the control simulation and decadal means for the final decade (2091-2100) in the scenario runs A2 and B2. Units are mm day^{-1}. Downward (upward) fluxes are positive (negative).

	CTRL	A2	A2-CTRL	B2	B2-CTRL
Globe					
Precipitation	2.81	2.86	0.02	2.86	0.02
Evaporation	-2.82	-2.87	0.02	-2.87	0.02
Land					
Precipitation	2.13	2.35	0.22	2.29	0.16
Evaporation	-1.43	-1.53	-0.10	-1.51	-0.08
Runoff	-0.66	-0.76	-0.10	-0.72	0.06
Snow accum. on glaciers	-0.05	-0.06	-0.01	-0.06	-0.01
Ocean					
Precipitation	3.09	3.06	-0.03	3.09	0.00
Evaporation	-3.39	-3.41	-0.02	-3.42	-0.03
Precipitation + evaporation	-0.30	-0.35	-0.05	-0.33	-0.03

ened by drought already in today's climate, in particular the southwestern part of the United States, the Mediterranean and the west coasts of South America, southern Africa and Australia. More precipitation than in present-day climate is simulated for large parts of the tropics.

In agreement with a number of models (e.g. Meehl and Washington, 1996), there is an El Niño-like precipitation anomaly pattern related to SST changes (Fig. 6). The dipole structure over the tropical Indian Ocean can be explained by a northward displacement of the precipitation pattern. Over the tropical Atlantic, on the other hand, precipitation decreases due to the eastward displacement of the Walker circulation, so that we find a dramatic decrease of precipitation over the northeastern part of Brazil with only one tenth of the present-day precipitation remaining. This displacement leads to a stabilization of the North Atlantic thermohaline circulation (see below) via the anomalous transfer of freshwater from the Atlantic to the Pacific, as discussed in Roeckner et al. (1999).

In both scenarios, we also find an increase of the Indian summer monsoon by approximately 30%, which is in agreement with Roeckner et al. (1999) but contradicts earlier findings by e.g. Lal et al. (1995), Meehl et al. (1996) and Mitchell and Johns (1997). A possible explanation is related to the fact that the direct effect depends on the change in sulfate aerosol (which is largest over the continental source regions), whereas the indirect effect is also reciprocally dependent to the number of cloud condensation nuclei (CCN). This implies that in regions with a high CCN number (continents), even a "saturation effect" is possible, so that the indirect effect is stronger over the ocean. Earlier experiments, such as Lal et al. (1995) have estimated a larger direct effect (factor of 2 compared to ours) which may explain the stronger effect on the monsoon.

Fig. 7 shows the percentage change in soil wetness for the last 30 years of the scenarios minus the present-day conditions. In DJF, we find an increase in soil wetness in the cold regions of the NH (Russia, Canada), whereas soil moisture decreases in temperate regions that are not generally snow-covered. In JJA, drying of the soil is simulated almost everywhere in the extratropics. An important exception are India and the slope of the Himalaya, where soil moisture increases by more than 30%.

5.3 Radiative and heat fluxes

Table 2 shows the components of the radiative budget for the control simulation and for the last decade (2091-2100) of both scenarios. As discussed by Roeckner et al. (1999), the clear-sky shortwave radiation at the top of the atmosphere increases due to changes in the albedo that are related to the melting of snow and ice. This increase is counteracted by an increase of clear-sky albedo that is caused by the tropospheric aerosols. The GSDIO experiment by Roeckner et al., forced by the IS92a emission scenario, ended in 2050. At this time, the direct aerosol effect is able to cancel the increase in absorbed shortwave radiation. In both scenario simulations discussed here, however, there is a decrease in sulfate emissions and thus burden (see Fig. 1) after about 2050. Consequently, during the second half of the period, the clear-sky albedo effect outweighs the direct aerosol effect.

The change in longwave clear-sky radiation is quite small. The increase in the clear-sky greenhouse effect that is caused largely by the moistening of the atmosphere is almost balanced by a large increase in surface emission due to surface warming.

Table 2: 300 year mean heat fluxes in the control simulation and decadal means for the final decade (2091-2100) in the scenario runs A2 and B2. Units are Wm^{-2}. Downward (upward) fluxes are positive (negative).

	CTRL	A2	A2-CTRL	B2	B2-CTRL
Top of atmosphere					
Shortwave clear sky	287.6	289.8	2.2	289.3	1.7
Longwave clear sky	-264.4	-262.4	2.0	-263.2	1.2
Surface emission	-398.1	-418.2	-20.1	-412.9	-14.8
Clear sky greenhouse effect	133.7	155.8	22.1	149.7	16.0
Shortwave cloud forcing	-49.8	-52.7	-2.9	-52.1	-2.3
Longwave cloud forcing	28.9	29.6	0.7	29.5	0.6
Net top of atmosphere radiation	2.3	4.3	2.0	3.5	1.2
Atmosphere					
Shortwave clear sky	72.0	78.9	6.9	77.2	5.2
Longwave clear sky	-190.9	-201.2	-10.3	-198.9	-8.0
Shortwave cloud forcing	17.1	16.9	-0.2	17.0	-0.1
Longwave cloud forcing	8.1	11.7	3.6	10.8	2.7
Net atmospheric radiation	-93.7	-93.7	0.0	-93.9	-0.2
Surface					
Sensible heat flux	-11.9	-10.3	1.6	-10.7	1.2
Latent heat flux	-81.9	-83.3	-1.4	-83.2	-1.3
Shortwave clear sky	215.6	210.8	-4.8	212.1	-3.5
Longwave clear sky	-73.5	-61.1	12.4	-64.3	9.2
Shortwave cloud forcing	-66.9	-69.6	-2.7	-69.0	-2.1
Longwave cloud forcing	20.8	17.9	-2.9	18.7	-2.1
Net surface radiation	96.0	98.0	2.0	97.4	1.4
Net surface heat flux	2.2	4.4	2.2	3.6	1.4

Changes in cloud radiative forcing can be related to changes in cloud amount and cloud water content. In a warmer atmosphere, clouds have a larger optical thickness, which diminishes the shortwave forcing and slightly enhances the longwave forcing, with the net change in forcing being negative. The atmospheric solar cloud forcing (difference of TOA and surface shortwave forcing) shows a small increase everywhere in the tropics (except over the tropical Pacific,

where 10 Wm^{-2} are exceeded) and a small decrease elsewhere. A distinct increase of atmospheric (=TOA-surface) longwave cloud forcing is evident after about 2040, with maximum values over the tropical Pacific (Fig. 12), caused by an increase in cloudiness and the Arctic, where we find the retreat of sea ice that was discussed in section 5.1.

In both experiments, the sensible heat flux is reduced, contributing to surface warming, while the latent heat flux increases, contributing to surface cooling. This is different to the GSDIO experiment (Roeckner et al., 1999) where both the sensible and latent heat fluxes, and hence evaporation and precipitation, are diminished due to the relatively high sulfur emissions in the IS92a scenario employed in GSDIO.

5.4 Sea level pressure and near-surface wind speed

As documented in Roeckner et al. (1999), global warming results in a systematic poleward shift of the climatological sea level pressure patterns. A very similar response is found in our experiments (Fig. 13). This leads to a significant increase of the westerlies around 60˚S (Fig. 14) throughout the year. Fig. 13 also shows a decrease of sea level pressure in the Arctic and slight strengthening of the Azores high. This leads to a rather strong increase in wind speed over the North Sea region. Furthermore, as Fig. 15 demonstrates, a greenhouse signal is visible in the North Atlantic Oscillation (NAO) towards higher (i.e., more zonal) index values.

6. Oceanic climate response

In this chapter, the response of the ocean to the radiative forcing from enhanced concentrations of greenhouse gases and aerosols is briefly described. This will mainly be done in terms of calculating the trend of different quantities, such as sea surface temperature (SST). Testing the statistical significance of these trends against natural variability is not a simple task, since the time scales of the oceanic processes involved is several decades and therefore comparable to the “signal” we are looking for. Therefore, a thorough analysis must involve also an assessment of the natural variability from the control run. This will be done in a later and more extended analysis.

6.1 Temperature

The most imminent consequence of the rising temperatures of the lower troposphere is a corresponding warming of the surface layer of the ocean. This can be seen in Fig. 16 showing the global average of the monthly mean sea surface temperature for the two scenarios where, in addition to the annual cycle, a steadily rising average temperature is seen. For scenario A2, the trend amounts to the value of 0.20 K/decade.

The geographical distribution of this trend is displayed in Fig. 17. Generally, the largest trends are found on the Northern Hemisphere and tropical regions. Over the North and Tropical Atlantic and Pacific Oceans large areas with values exceeding 0.2 K are found. West of Peru a particular large value is found, corresponding to a permanent El Niño situation. Also the Barents Sea experience a large warming. In the southern basins the values are modest, except for the Indian Ocean. In the Southern Ocean areas with altering small positive and negative trends are found. This is probably connected to variability in the Antarctic Circumpolar Current with time scale of several decades which is seen in the experiment. Southeast of Australia an area with a large positive trend is found. The reason for this is not known.

Also in the interior of the ocean warming is found, although at a rate depending of depth. This is illustrated in Fig. 18. From this figure it can be seen that water masses at intermediate depths around 1000 m are not affected much, while the warming again becomes larger at deeper levels. The trend in the potential temperature at 3000 m depth (not shown) is largest in the Southern ocean and in the North Atlantic. Only in the North Atlantic, this can be understood by vertical advection of heated surface water. In the Southern Ocean the surface heating is modest and other explanations must be sought.

6.2 Salinity

The global average of the sea surface salinity is shown in Fig. 19. For both scenarios, a freshening is seen until about year 2030, after which the average SSS is approximately constant. The average trends in SSS is -0.037 psu/decade for the A2 scenario. The geographical distribution of this signal is depicted in Fig. 20. Generally the largest changes are found on the Northern Hemisphere. The Northern and tropical Atlantic and the Barents Sea is becoming more saline. The Arctic areas north of 80°N are getting fresher due to the melting of ice, except of some areas north of the of the Eastern Siberian and Canadian.

6.3 Thermohaline circulation

Rahmstorf and Ganopolsky (1999) find generally a slowing down of the meridional overturning in the Atlantic (THC) in the case of global warming, which is caused by the lowering of the surface water density either by the increased warming or an increase of the fresh water flux in the mid-latitudes (Mikolajewicz and Voss, 2000; Dixon et al, 1999). A comparison of eight model simulations by Cubasch and Fischer-Bruns (2000) show that the responses of the THC to an increase of greenhouse gas concentrations ranges from a strong decline of around 30% by the model of CSIRO (Gordon and O'Farrell, 1997) in 100 years to virtually no response (ECHAM4/OPYC; Latif et al, 2000).

Fig. 21 shows a decay of the THC in A2 during the simulation. Compared to the uncoupled control run and the initial phase of GSDIO (where the forcing is still very small), these changes appear to be within the range of natural THC variability. As shown by Latif et al. (2000), the stability of the THC in this particular model is caused by a poleward transport of anomalously saline water from the tropical Atlantic. This remote effect is able to compensate for the local effects in the North Atlantic which tend to decrease the density of the surface water through warming and increase in freshwater flux.

7. Conclusions

We have used a coupled atmosphere/ocean general circulation model to study the time-dependent climate response to changing concentrations of greenhouse gases and aerosols according to the new IPCC SRES scenarios A2 and B2. The results of these experiments are compared to an unforced 300 year control experiment. The changes in the final three decades of the scenario simulations (2071-2100) are furthermore compared to the simulation of present-day climate (1961-1990).

Similarly to previous experiments, we find that greenhouse warming is reduced when aerosol effects come into play. However, sulfur emissions are lower than in the IS92a scenario. So the aerosol cooling effect can be outweighed by the greenhouse warming effect, which leads to a stronger temperature rise than in the GSDIO experiment by Roeckner et al. (1999).

This result shows that there still are quite large difficulties and uncertainties in such a kind of model simulation. These are partially due to oversimplifications in the model, in particular concerning the radiative properties of aerosols and therefore the indirect aerosol effect. However, another inherent problem is the uncertainty in the scenarios themselves. This is in particular the case for short-lived substances with an inhomogeneous spatial and temporal distribution, such as aerosols. Changes in the emissions of these substances can therefore, on a decadal horizon, exert a rather large effect on anthropogenic climate change.

Acknowledgments

The authors thank Eigil Kaas, Lennart Bengtsson, Johann Feichter, Bennert Machenhauer, Jan-Peter Schulz and Wilhelm May for helpful discussions and suggestions that helped to improve the manuscript. Assistance from Monika Esch, Reinhard Budich and Niels Hansen is gratefully acknowledged. The model simulations were carried out at DMI's Danish Climate Centre in Copenhagen. Special thanks go to the computer departments of the Danish Meteorological Institute and the German Climate Computing Centre (DKRZ) for their technical assistance. This research was supported by the Danish Climate Centre.

References

Adams, P.J., J.H. Seinfeld, D.M. Koch, L. Mickley and D. Jacob, 2000: General circulation model assessment of direct radiative forcing by the sulfate-nitrate-ammonium-water inorganic aerosol system. *J. Geoph. Res.* (accepted).

Bacher, A., J. Oberhuber and E. Roeckner, 1998: ENSO dynamics and seasonal cycle in the tropical Pacific as simulated by the ECHAM4/OPYC coupled general circulation model. *Clim. Dyn.* **14**, 431-450.

Chuang, C.C., J.E. Penner, J.M. Prospero, K.E. Grant and G.H. Rau, 2000:Effects of anthropogenic aerosols on cloud susceptibility: a sensitivity study of radiative forcing to aerosol characteristics and global concentration. *J. Geoph. Res.* (submitted).

Claussen, M., U. Lohmann, E. Roeckner and U. Schulzweida, 1994: A global data set of land-surface parameters. *Max-Planck-Institut für Meteorologie* Report No. **135**, 34 pp.

Cooke, W.F., C. Liousse, H. Chachier and J. Feichter, 1999: Construction of a 1°x1° fossil-fuel emission dataset for carbonaceous aerosols and implementation and radiative effect in the ECHAM-4 model. *J. Geoph. Res.* **104**, 22137-22162.

Cubasch, U. and I. Fischer-Bruns, 2000: An intercomparison of scenario simulations performed with different OAGCMs. Proc. RegClim Seminar, Jevnaker, Norway, 8.-9.5. 2000.

Dixon, K.W., T.L. Delworth, M.J. Spelman and R.J. Stouffer, 1999: The influence of transient surface fluxes on North Atlantic overturning coupled GCM climate change experiments. *Geoph. Res. Lett.* **26**, 1885-1888.

Feichter, J., E. Kjellström, H. Rodhe, F. Dentener, J. Lelieveld and G.J. Roelofs, 1996: Simulation of the tropospheric sulfur cycle in a global climate model. *Atm. Env.* **30**, 1693-1707.

Feichter, J., U. Lohmann and I. Schult, 1997: The atmospheric sulfur cycle and its impact on the shortwave radiation. *Clim. Dyn.* **13**, 235-246.

Fouquart, Y. and B. Bonnel, 1980: Computations of solar heating of the Earth‘s atmosphere: A new parameterization. *Beitr. Phys. Atmos.* **53**, 35-62.

Giorgetta, M. and M. Wild, 1995: The water vapour continuum and its representation in ECHAM4. *Max-Planck-Institut für Meteorologie* Report No. **162**, 38 pp.

Gordon, H.B. and S.P. O'Farrell, 1997: Transient climate change in the CSIRO coupled model with dynamic sea ice. *Mon. Wea. Rev.* **125**, 875-907.

Graf, H.-F., J. Feichter and B. Langmann, 1997: Volcanic sulfur emissions: Estimates of source strength and its contribution to the global sulfate distribution. *J. Geoph. Res.* **102**, 10727-10738.

Grant, K.E., C.C. Chuang, A.S. Grossman and J.E. Penner, 1999: Modeling the spectral optical properties of ammonium sulfate and biomass aerosols: Parameterization of relative humidity effects and model results. *Atm. Env.* **33**, 2603-2620.

Hansen, J.E., M. Sato and R. Ruedy, 1997a: Radiative forcing and climate response. *J. Geophys. Res*. **102**, 6831-6864.

Hansen, J.E., M. Sato, R. Ruedy, A. Lacis, K. Asamoah, K. Beckford, S. Borenstein, E. Brown, B. Cairns, B. Carlson, B. Curran, S. de Castro, L. Druyan, P. Etwarrow, T. Ferede, M. Fox, D. Gaffen, J. Glascoe, H. Gordon, S. Hollandsworth, X. Jiang, C. Johnson, N. Lawrence, L. Lean, J. Lerner, K. Lo, J. Logan, A. Luckett, M.P. McCormick, R. McPeters, R. Miller, P. Minnis, I. Ramberron, G. Russell, P. Russell, P. Stone, I. Tegen, S. Thomas, L. Thomason, A. Thompson, J. Wilder, R. Willson and J. Zawodny, 1997b: Forcings and chaos in interannual to decadal climate change. *J. Geophys. Res.* **102**, 25679-25720.

Hansen, J., M. Sato, R. Ruedy, A. Lacis and V. Oinas, 2000: Global warming in the twenty-first century: An alternative scenario. *Proc. Natl. Acad. Sci. USA* **97**, 9875-9880.

Haywood, J.M. and V. Ramaswamy, 1998: Global sensitivity studies of the direct radiative forcing due to anthropogenic sulfate and black carbon aerosols. *J. Geoph. Res.* **103**, 6043-6058.

Haywood, J.M. and O. Boucher, 2000: Estimates of the direct and indirect radiative forcing due to tropospheric aerosols: a review. *Rev. Geoph.*, in press.

Intergovernmental Panel on Climate Change (IPCC), 1996: *Climate Change 1995: The Science of Climate Change*, J.T. Houghton, L.G. Meira Filho, B.A. Callander, N. Harris, A. Kattenberg and K. Maskell (eds.), 572 pp., Cambridge Univ. Press, New York, 1996.

Jacobson, M.Z., 2000: A physically-based treatment of elemental carbon optics: Implications for global direct forcing of aerosols. *Geoph. Res. Lett.* **27**, 217-220.

Jacobson, M.Z., 2000: Global direct radiative forcing due to multicomponent anthropogenic and natural aerosols. *J. Geoph. Res.* (accepted).

Jones, A. and A. Slingo, 1996: Predicting cloud-droplet effective radius and indirect sulphate aerosol forcing using a general circulation model. *Q. J. Roy. Met. Soc.* **122**, 1573-1595.

Jones, A., D.L. Roberts and M.J. Woodage, 1999: The indirect effects of anthropogenic sulphate aerosol simulated using a climate model with an interactive sulphur cycle. *Hadley Centre Tech. Note* **14**, 38 pp.

Kattenberg, A., F. Giorgi, H. Grassl, G.A. Meehl, J.F.B. Mitchell, R.J. Stouffer, T. Tokioka, A.J. Weaver and T.M.L. Wigley, 1996: Climate models - projections of future climate, in: Climate Change 1995: *The science of climate change*, J.T. Houghton et al. (eds.), Cambridge University Press, Cambridge 1995, 285-357.

Lal, M., U. Cubasch, R. Voss and J. Waszkewitz, 1995: Effect of transient increase in greenhouse gases and sulphate aerosols on monsoon climate. *Current Sci.* **69**, 752-763.

Latif, M., E. Roeckner, U. Mikolajewicz and R. Voss, 2000: Tropical stabilization of the thermohaline circulation in a greenhouse warming simulation. *J. Climate* **13**, 1809-1813.

Lohmann, U., J. Feichter, J.E. Penner and R. Leaitch, 2000: Indirect effect of sulfate and carbonaceous aerosols: A mechanistic treatment. *J. Geophys. Res*. **105**, 12193-12206.

Machenhauer, B., M. Windelband, M. Botzet, J.H. Christensen, M. Déqué, R.G. Jones, P.M. Ruti and G. Visconti, 1998: Validation and Analysis of Regional Present-day Climate and Climate Change. Simulations over Europe. *Max-Planck-Institut für Meteorologie* Report **275**, 91 pp.

May, W., 1999: A time-slice experiment with the ECHAM4 A-GCM at high resolution: The experimental design and the assessment of climate change as compared to a greenhouse gas experiment with ECHAM4/OPYC at low resolution. *Danish Meteorological Institute Report* **99-2**, Copenhagen.

Meehl, G.A. and W.M. Washington, 1996: El Niño-like climate change in a model with increased atmospheric CO_2 concentrations. *Nature* **382**, 56-60.

Meehl, G.A., D.J. Erickson III, B.P. Briegleb and P.J. Jaumann, 1996: Climate change from increased CO_2 and direct and indirect effects of sulfate aerosols. *Geoph. Res. Lett.* **23**, 3755-3758.

Mikolajewicz, U. and R. Voss, 2000: The role of the individual air-sea flux components in CO_2 induced changes of the oceans circulation and climate. *Clim. Dyn.* **16**, 627-642

Miller, M.J., T.N. Palmer and R. Swinbank, 1989: Parameterization and influence of sub-grid scale orography in general circulation and numerical weather prediction models. *Met. Atm. Phys.* **40**, 84-109.

Miller, R. and I. Tegen, 1998: Climate response to soil dust aerosols. *J. Climate* **11**, 3247-3267.

Mitchell, J.F.B. and T.C. Johns, 1997: On the modification of greenhouse gas warming by sulphate aerosols. *J. Climate* **10**, 245-267.

Morcrette, J.-J., L. Smith and Y. Fouquart, 1986: Pressure and temperature dependence of the absorption in longwave radiation parameterizations. *Beitr. Phys. Atmos.* **59**, 455-469.

Nakicenovic, N., J. Alcamo, G. Davis, B. de Vries, J. Fenhann, S. Gaffin, K. Gregory, A. Grübler, T.Y. Jung, T. Kram, E.L. La Rovere, L. Michaelis, S. Mori, T. Morita, W. Pepper, H. Pitcher, L. Price, K. Raihi, A. Roehrl, H.-H. Rogner, A. Sankovski, M. Schlesinger, P. Shukla, S. Smith, R. Swart, S. van Rooijen, N. Victor and Z. Dadi, 2000: *IPCC special report on emissions scenarios.* Cambridge University Press, Cambridge, UK, 599 pp.

Nordeng, T.E., 1994: Extended versions of the convective parameterization scheme at ECMWF and their impact on the mean and transient activity of the model in the tropics. ECMWF Res. Dep. Tech. Mem. **206**, European Centre for Medium Range Weather Forecasts, Reading, UK.

Oberhuber, J.M., 1993: Simulation of the Atlantic circulation with a coupled sea ice-mixed layer-isopycnal general circulation model. Part I: Model description. *J. Phys. Oceanogr.* **22**, 808-829.

Penner, J.E., C.C. Chuang and K. Grant, 1998: Climate forcing by carbonaceous and sulfate aerosols. *Clim. Dyn.* **14**, 839-851.

Rahmstorf, S. and A. Ganopolsky, 1999: Long-term global warming scenarios computed with an efficient coupled climate model. *Clim. Change* **43**, 353-367.

Ramaswamy, V., M.D. Schwarzkopf and W.J. Randel, 1996: Fingerprint of ozone depletion in the spatial and temporal pattern of recent lower-stratospheric cooling. *Nature* **382**, 616-618.

Rockel, B. E. Raschke and B. Weyres, 1991: A parameterization of broad band radiative transfer properties of water, ice and mixed clouds. *Beitr. Phys. Atm.* **64**, 1-12.

Roeckner, E., 1995: Parameterization of cloud radiative properties in the ECHAM4 model. In: *Proceedings of the WCRP Workshop on „Cloud Microphysics Parameterizations in Global Atmospheric Circulation Models“*, May 23-25, 1995, Kananaskis, Alberta, Canada, WCRP Report No. **90**, 105-116, WMO-TD-No. 713.

Roeckner, E., K. Arpe, L. Bengtsson, M. Christoph, M. Claussen, L. Dümenil, M. Esch, M. Giorgetta, U. Schlese and U. Schulzweida, 1996: The atmospheric general circulation model ECHAM-4: Model description and simulation of present-day climate. Max-Planck-Institut für Meteorologie, Report No. **218,** 90pp.

Roeckner E., L. Bengtsson, J. Feichter, J. Lelieveld and H. Rodhe, 1999: Transient climate change simulations with a coupled atmosphere-ocean GCM including the tropospheric sulfur cycle. *J. Climate* **12**, 3004-3032.

Roelofs, G.-J. and J. Lelieveld, 1995: Distribution and budget of O_3 in the troposphere calculated with a chemistry-general circulation model. *J. Geoph. Res*. **100**, 20983-20998.

Rotstayn, L.D., 1999: Indirect forcing by anthropogenic aerosols: A GCM calculation of the effective radius and cloud lifetime effects. *J. Geoph. Res.* **104**, 9369-9380.

Shine, K.P. and P.M. de F. Forster, 1999: The effects of human activities on radiative forcing of climate change: a review of recent developments. *Glob. Planet. Change* **20**, 205-225.

Stenchikov, G.L. and A. Robock, 1995: Diurnal asymmetry of climatic response to increased CO_2 and aerosols: Forcing and feedbacks. *J. Geoph. Res.* **100**, 26211-26227.

Tiedtke, M., 1989: A comprehensive mass flux scheme for cumulus parameterization in large-scale models. *Mon. Wea. Rev.* **117**, 1779-1800.

Williamson, D.L. and P.J. Rasch, 1994: Water vapor transport in the NCAR CCM2. *Tellus* **46A**, 34-51.

Figure captions

Fig. 1: Upper panel: Temporal evolution of annual mean radiative forcing [W m^{-2}] from well-mixed greenhouse gases. Lower panel: Decadal mean sulfur emissions [Tg S a^{-1}].

Fig. 2: Geographical distribution of sulfur emissions [mg S m^{-2} day^{-1}] for (a) 1990, (b) 2030, (c) 2070 and (d) 2100. Top: scenario A2, bottom: scenario B2.

Fig. 3: Temporal evolution of the annual global mean surface air temperature anomalies [K] from the mean of the control run for the simulations GSDIO (Roeckner et al., 1999), A2 and B2. Observed temperatures relative to the average 1860-1900 are also given. All data is smoothed by 5 year running means.

Fig. 4: Changes [K] in mean surface air temperature (a) in DJF, (b) in JJA for the period 2071-2100 compared to the period 1961-1990.

Fig. 5: As Fig. 4, for diurnal temperature range.

Fig. 6: Precipitation (a) in DJF, (b) in JJA for the period 2071-2100 compared to the period 1961-1990, expressed as percentage of the precipitation amount 1961-1990.

Fig. 7: As Fig. 4, for soil moisture [cm water column].

Fig. 8: As Fig. 4, for cloud cover [%].

Fig. 9: Temporal evolution of Arctic sea-ice cover [10^6 km^2] for the simulations GSDIO (Roeckner et al., 1999), A2 and B2.

Fig. 10:Percentage reduction in sea-ice volume (a) in DJF, (b) in JJA for the period 2071-2100 compared to the period 1961-1990.

Fig. 11:Temporal evolution of (a) near-surface temperature [°C], (b) sea level pressure [hPa], (c) precipitation [mm day^{-1}] and (d) sea-ice cover [10^6 km^2] in the Barents Sea region (70°–80°N, 30°–50°E).

Fig. 12:As Fig. 4, for atmospheric (=TOA-surface) longwave cloud forcing [W m^{-2}].

Fig. 13:As Fig. 4, for sea level pressure [hPa].

Fig. 14:As Fig. 4, for 10 m wind speed [m s^{-1}].

Fig. 15:Time series of the NAO index, calculated from the normalized DJF pressure difference Gibraltar (36°N, 6°W) minus Stykkisholmur/Iceland (65°N, 23°W). A nine year running mean has been applied.

Fig. 16:Evolution of global average of the monthly mean SST [°C] for scenario A2.

Fig. 17:Geographical distribution of the average trend in SST over the period 1990-2090 for scenario A2. Contour interval: 0.1 K/decade.

Fig. 18:Vertical cross section of globally averaged monthly mean temperature trends [K/decade] for scenario A2.

Fig. 19:Evolution of global average of the monthly mean SSS [psu] for scenario A2.

Fig. 20:Geographical distribution of the average trend in SSS over the period 1990-2090 for scenario A2. Contour interval: 0.1 psu/decade.

Fig. 21:Time series of the Atlantic meridional overturning circulation [Sv], defined as the maximum value of the transport stream function over the area 30°S to 90°N for the control simulation and the scenarios IS92a (GSDIO experiment of Roeckner et al., 1999), A2 and B2.

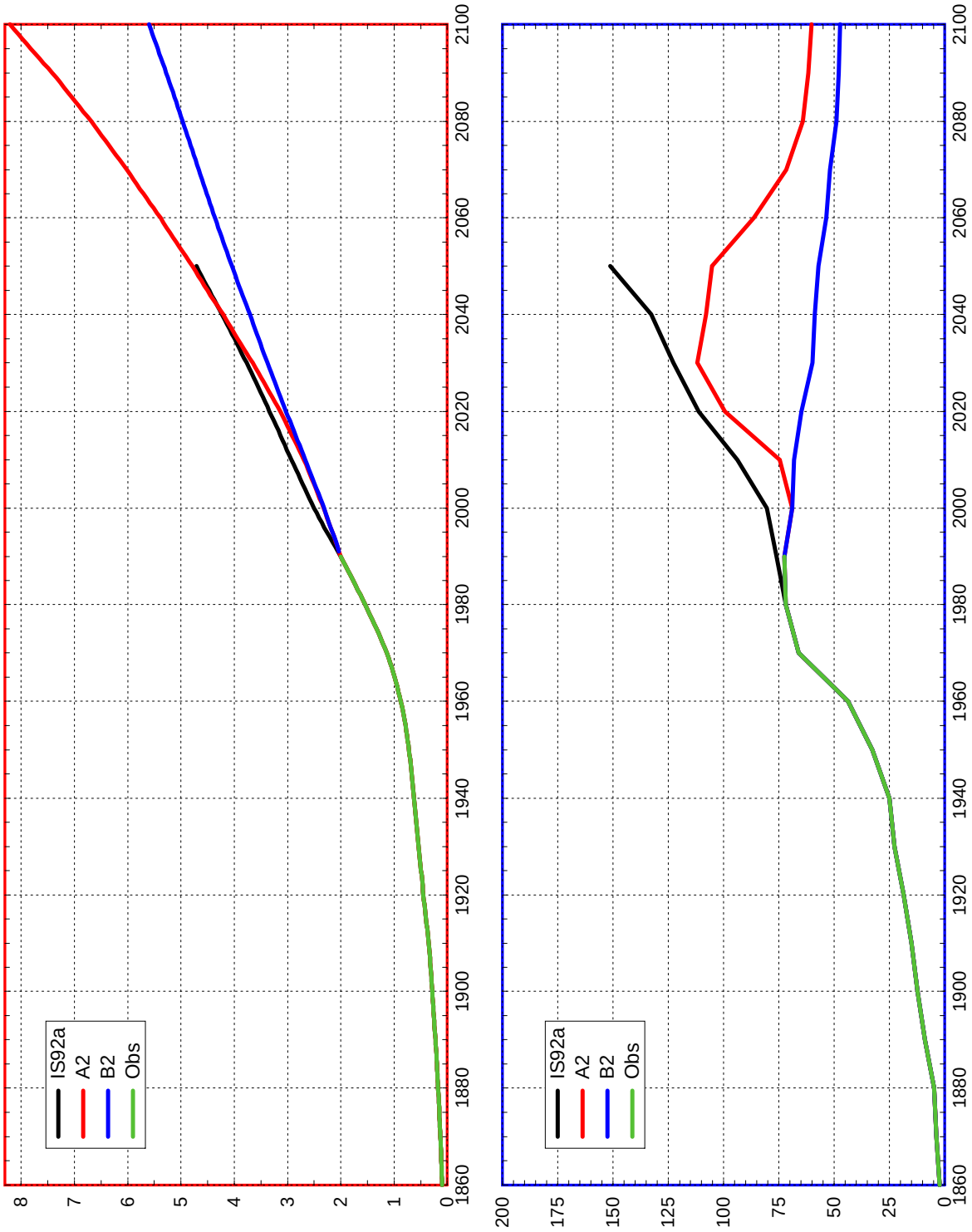

Fig. 1: Upper panel: Temporal evolution of annual mean radiative forcing [W m^{-2}] from well-mixed greenhouse gases. Lower panel: Decadal mean sulfur emissions [Tg S a^{-1}].

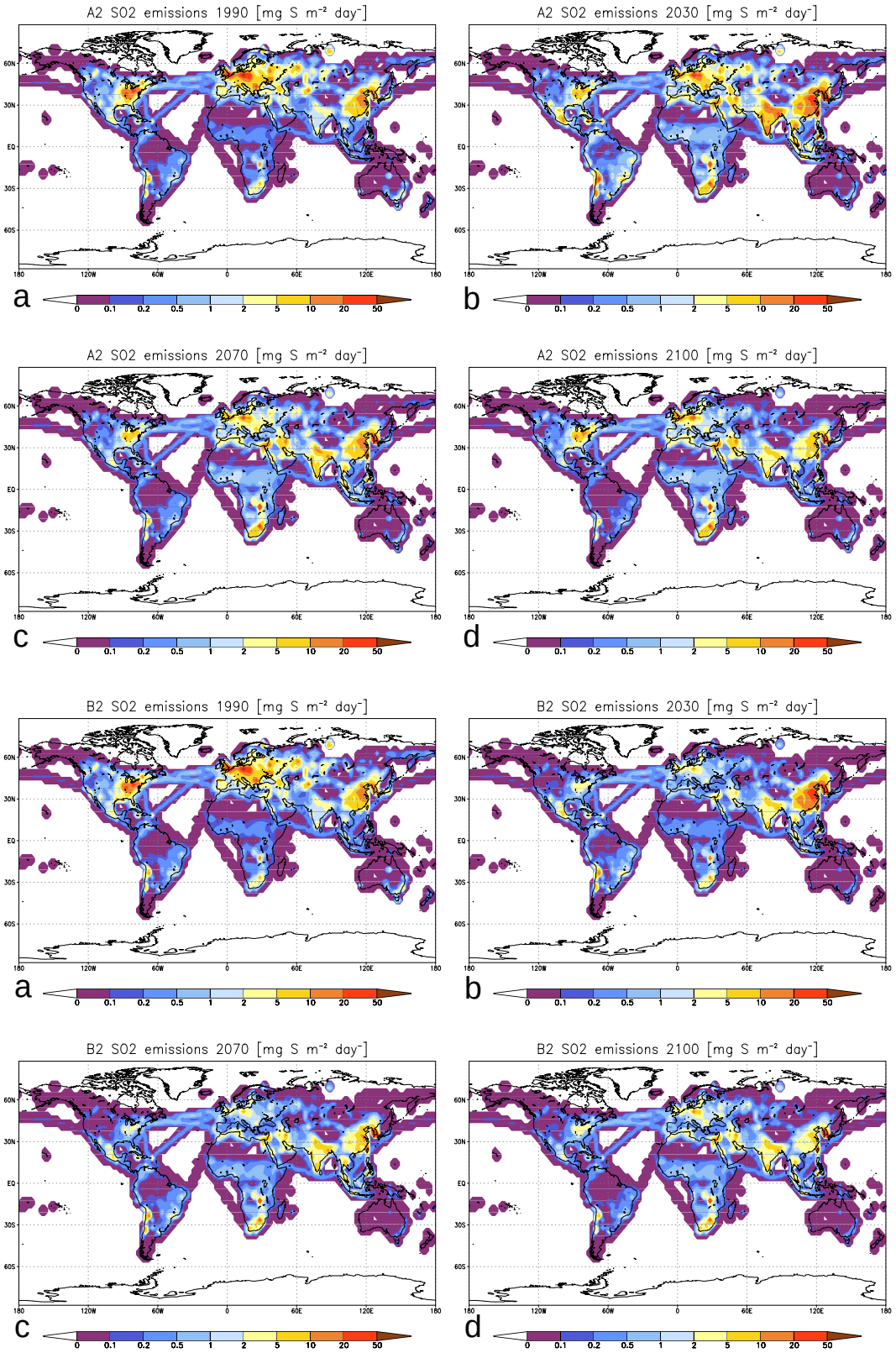

Fig. 2: Geographical distribution of sulfur emissions [mg S m^{-2} day^{-1}] for (a) 1990, (b) 2030, (c) 2070 and (d) 2100. Top: scenario A2, bottom: scenario B2.

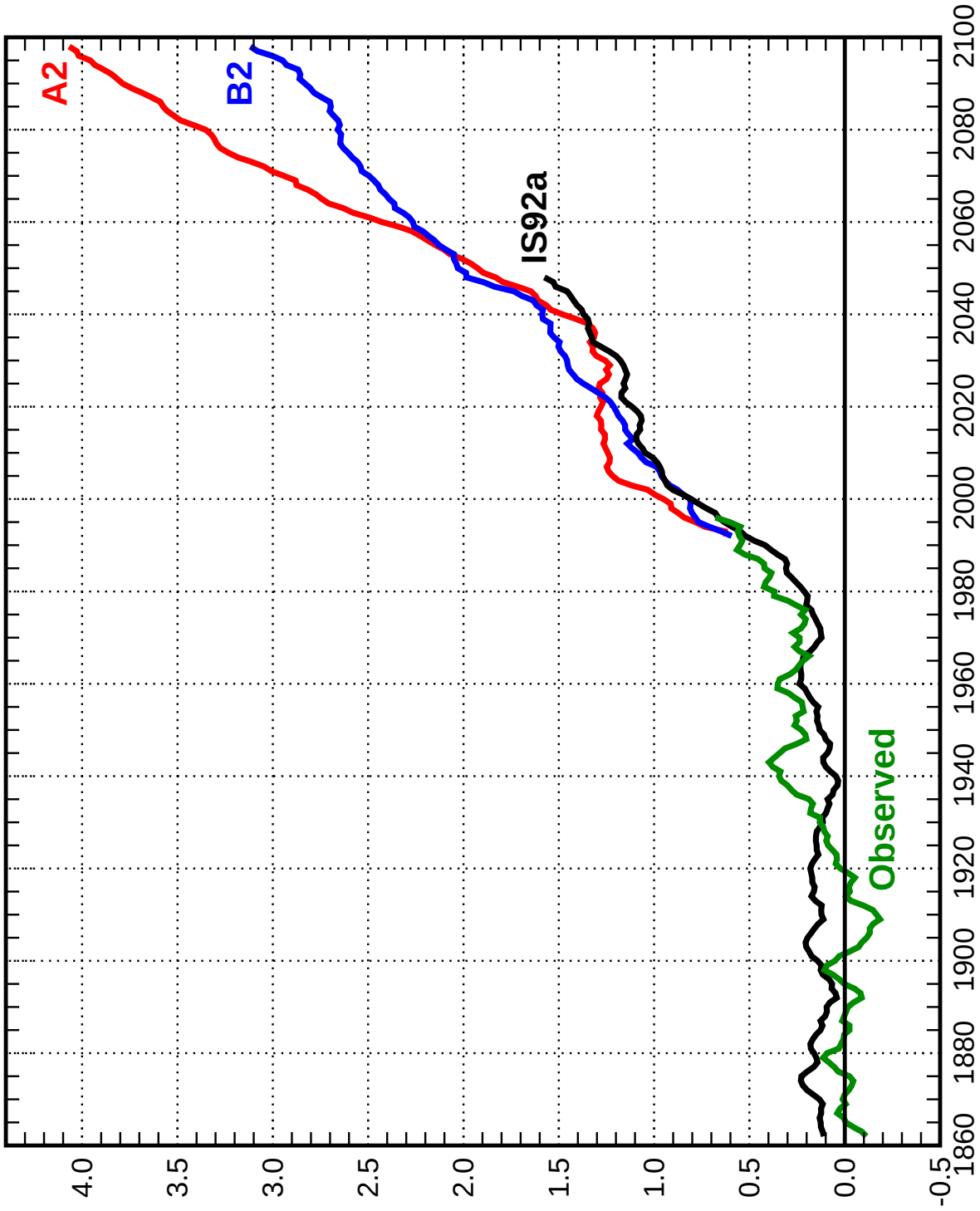

Fig. 3: Temporal evolution of the annual global mean surface air temperature anomalies [K] from the mean of the control run for the simulations GSDIO (Roeckner et al., 1999), A2 and B2. Observed temperatures relative to the average 1860-1900 are also given. All data is smoothed by 5 year running means.

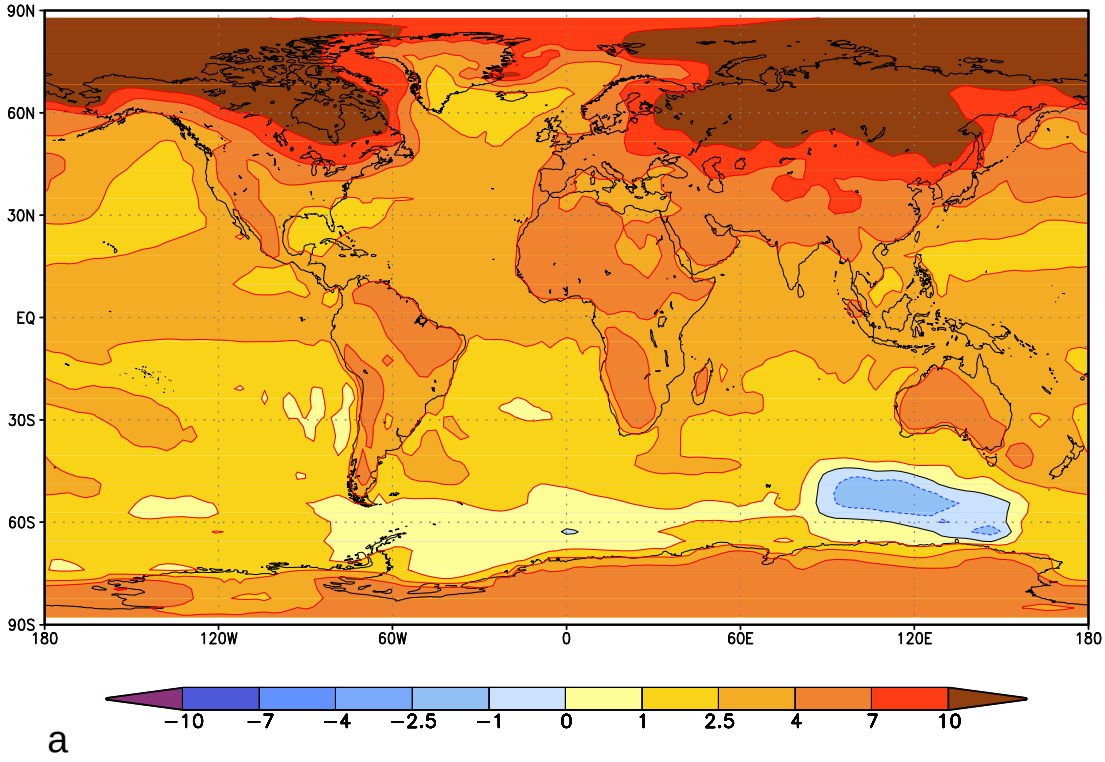

a

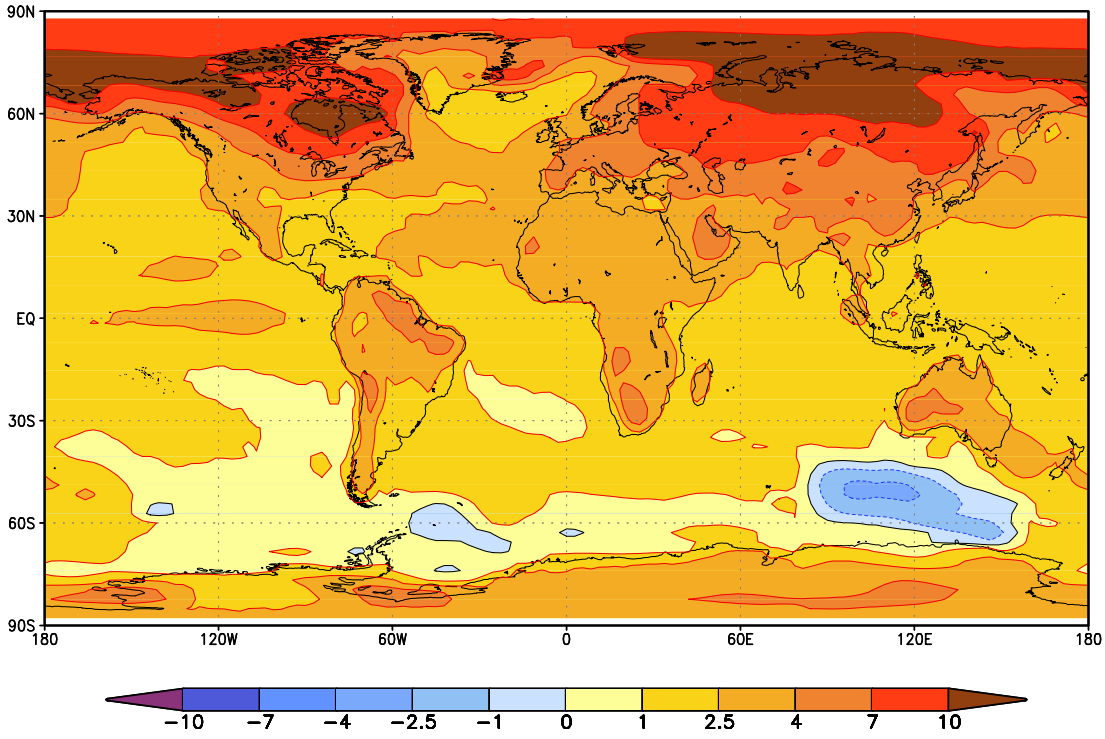

Fig. 4: Changes [K] in mean surface air temperature (a) in DJF, (b) in JJA for the period 2071-2100 compared to the period 1961-1990. Top: scenario A2, bottom: scenario B2.

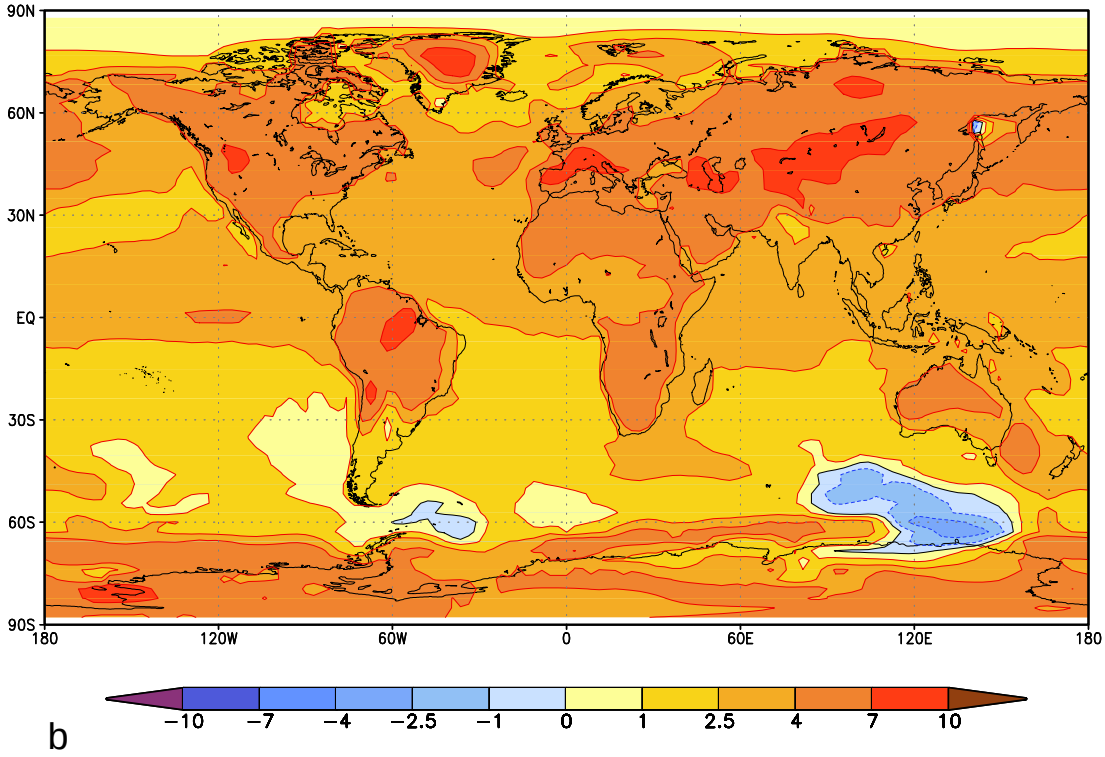

b

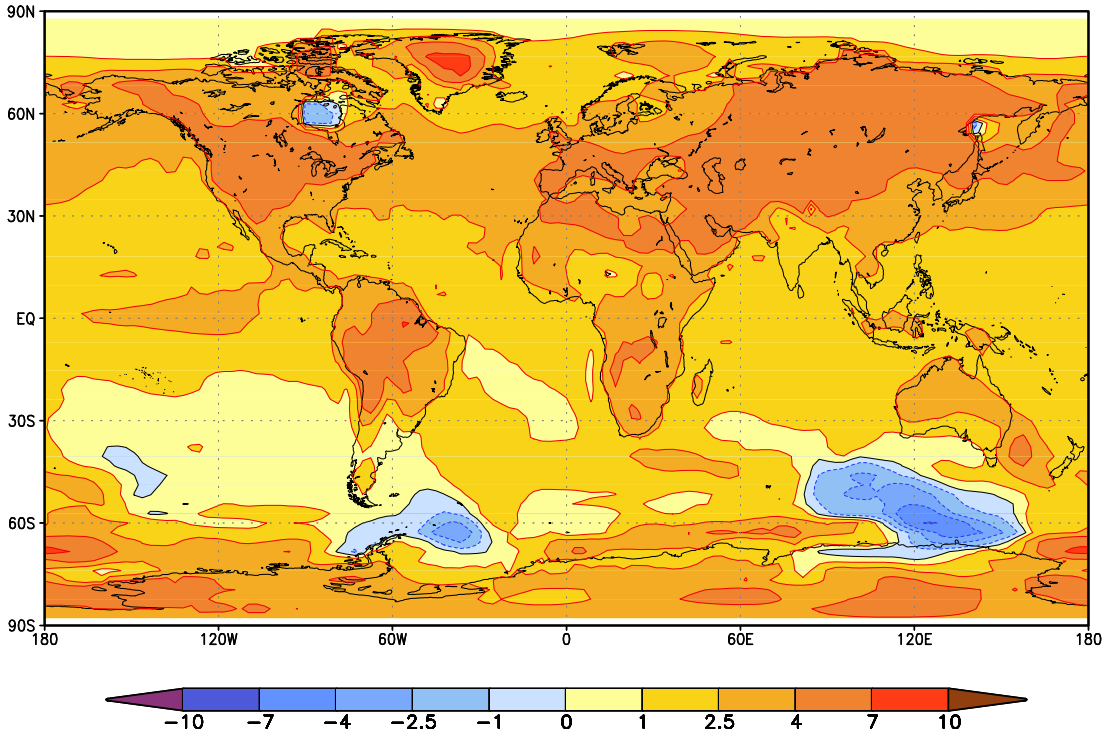

Fig. 4 (continued)

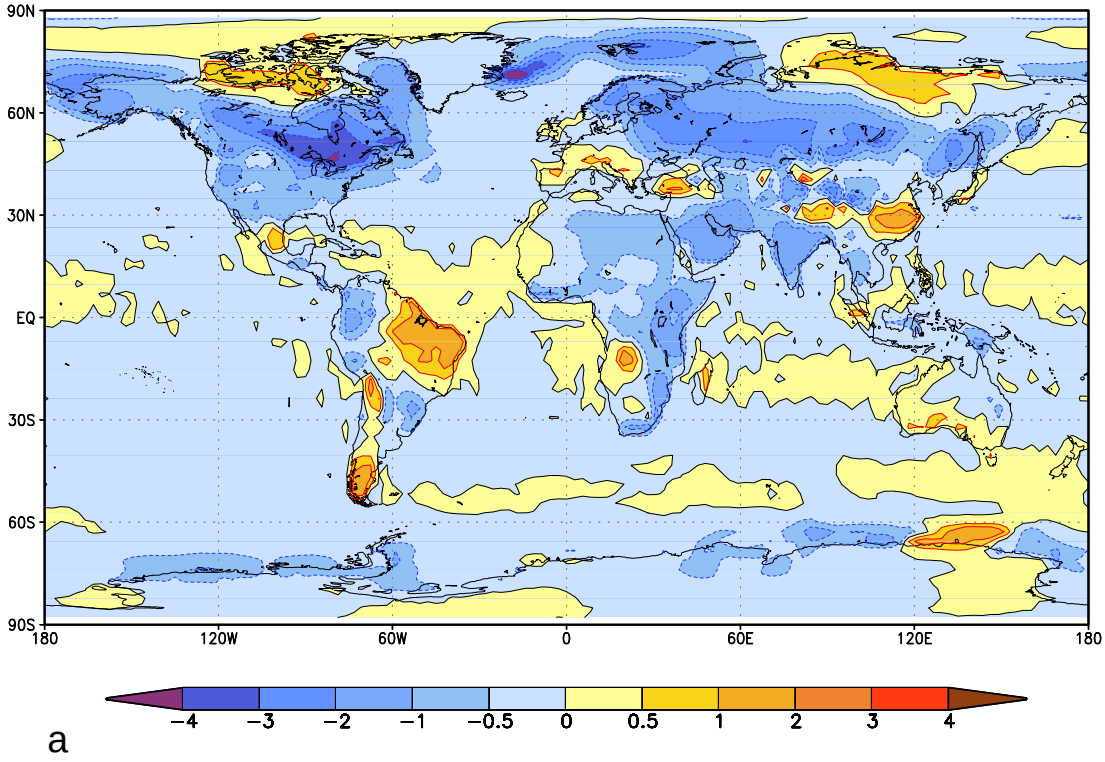

a

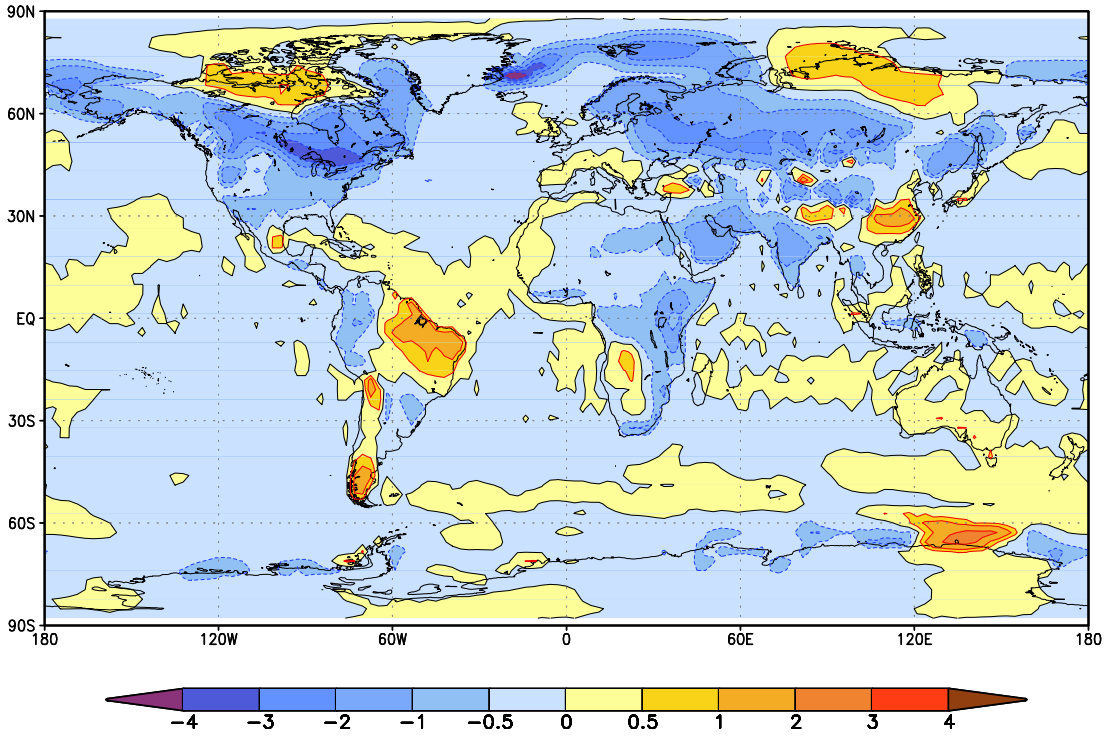

Fig. 5: As Fig. 4, for diurnal temperature range.

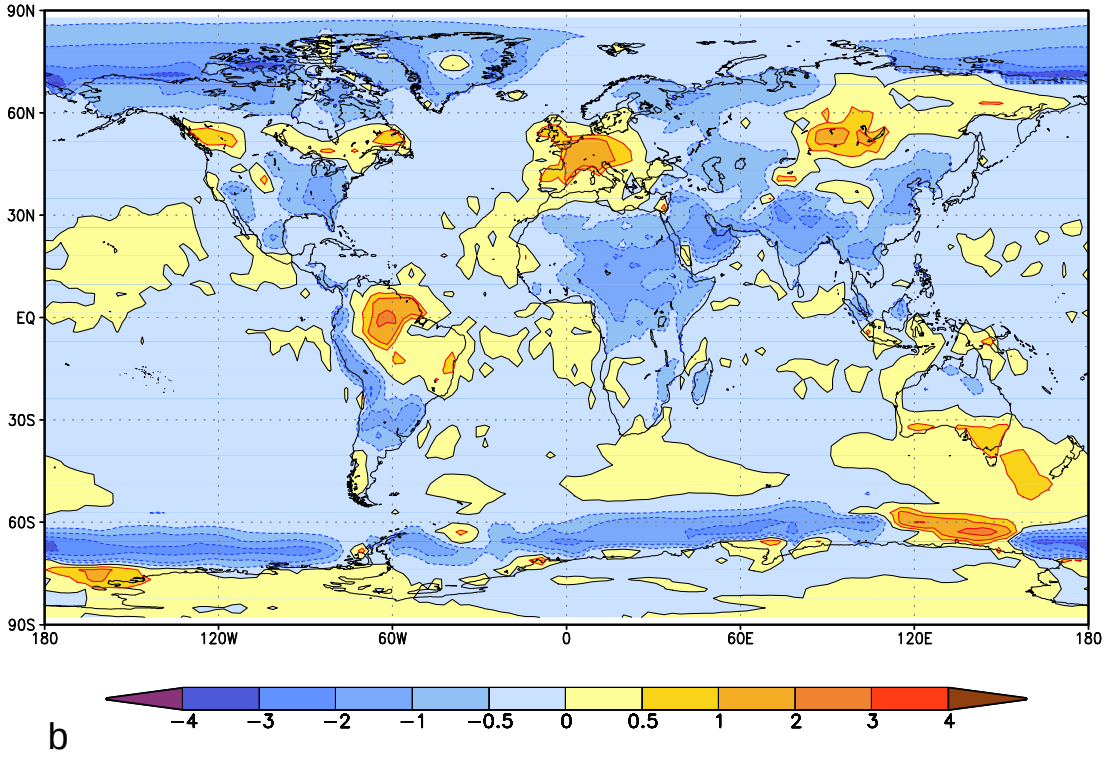

b

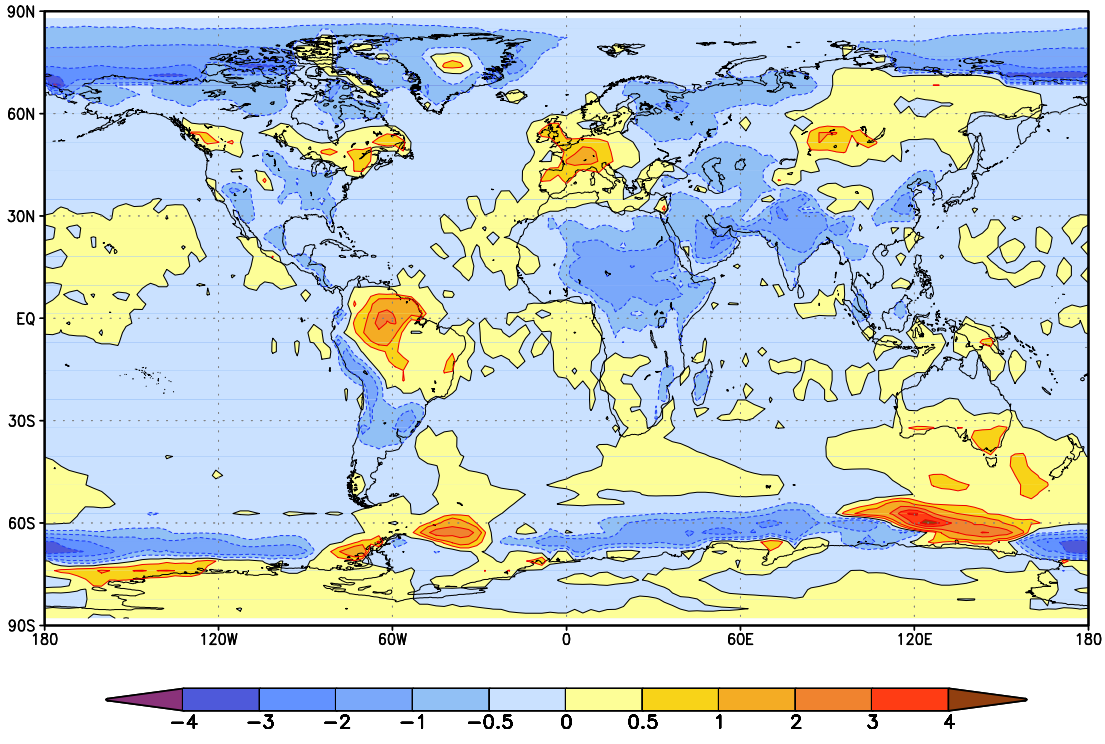

Fig. 5 (continued)

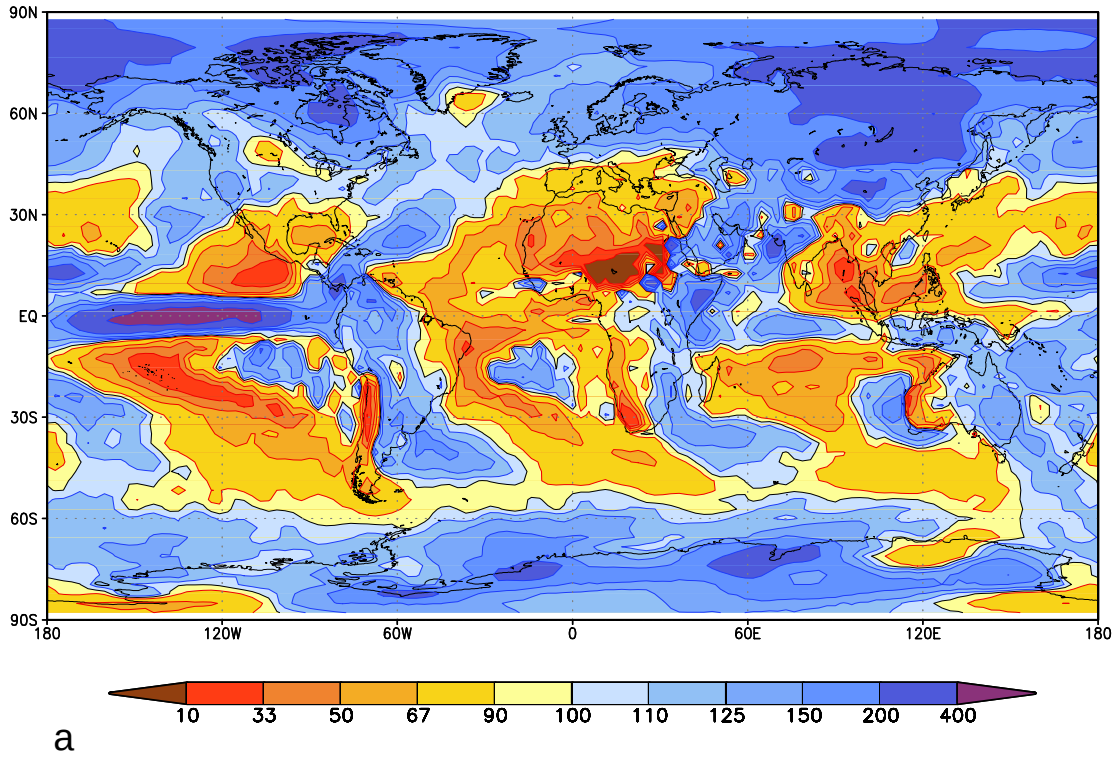

a

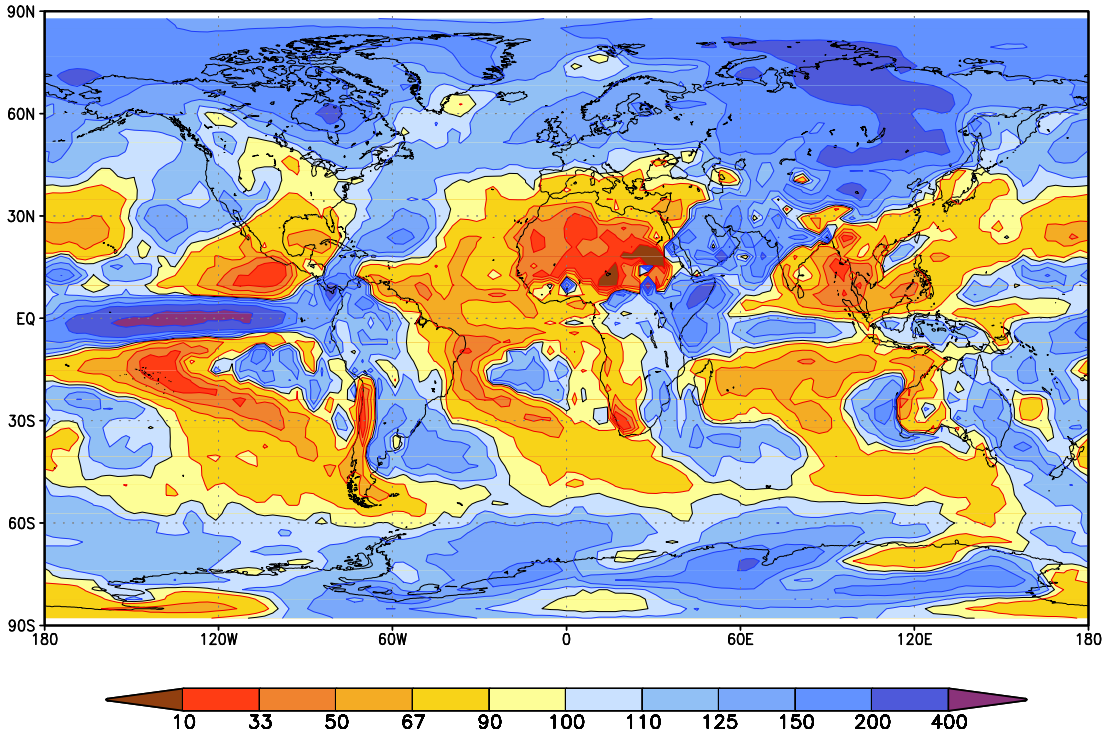

Fig. 6: Precipitation (a) in DJF, (b) in JJA for the period 2071-2100 compared to the period 1961-1990, expressed as percentage of the precipitation amount 1961-1990. Top: scenario A2, bottom: scenario B2.

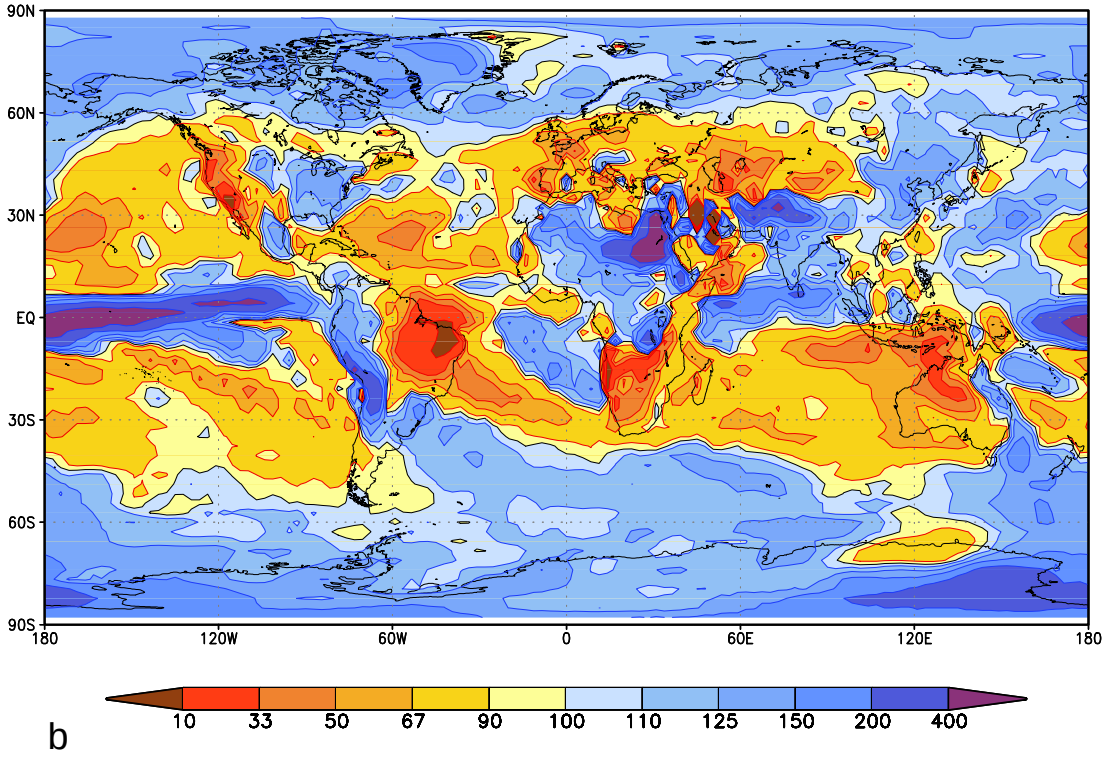

b

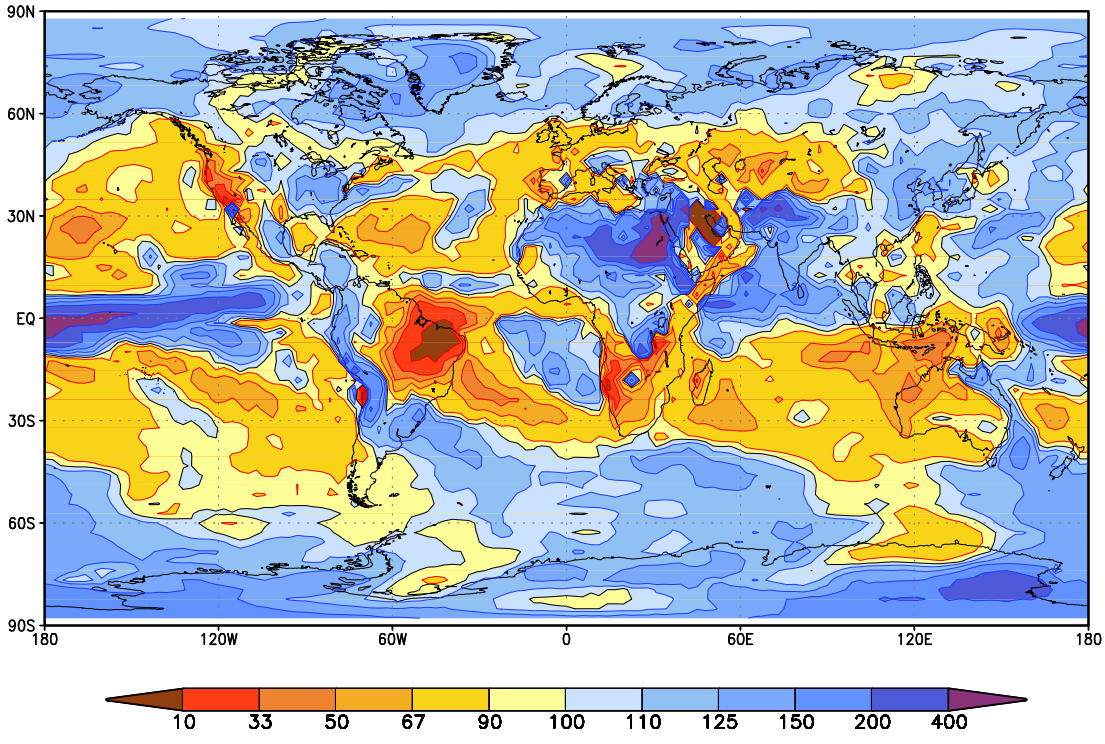

Fig. 6 (continued)

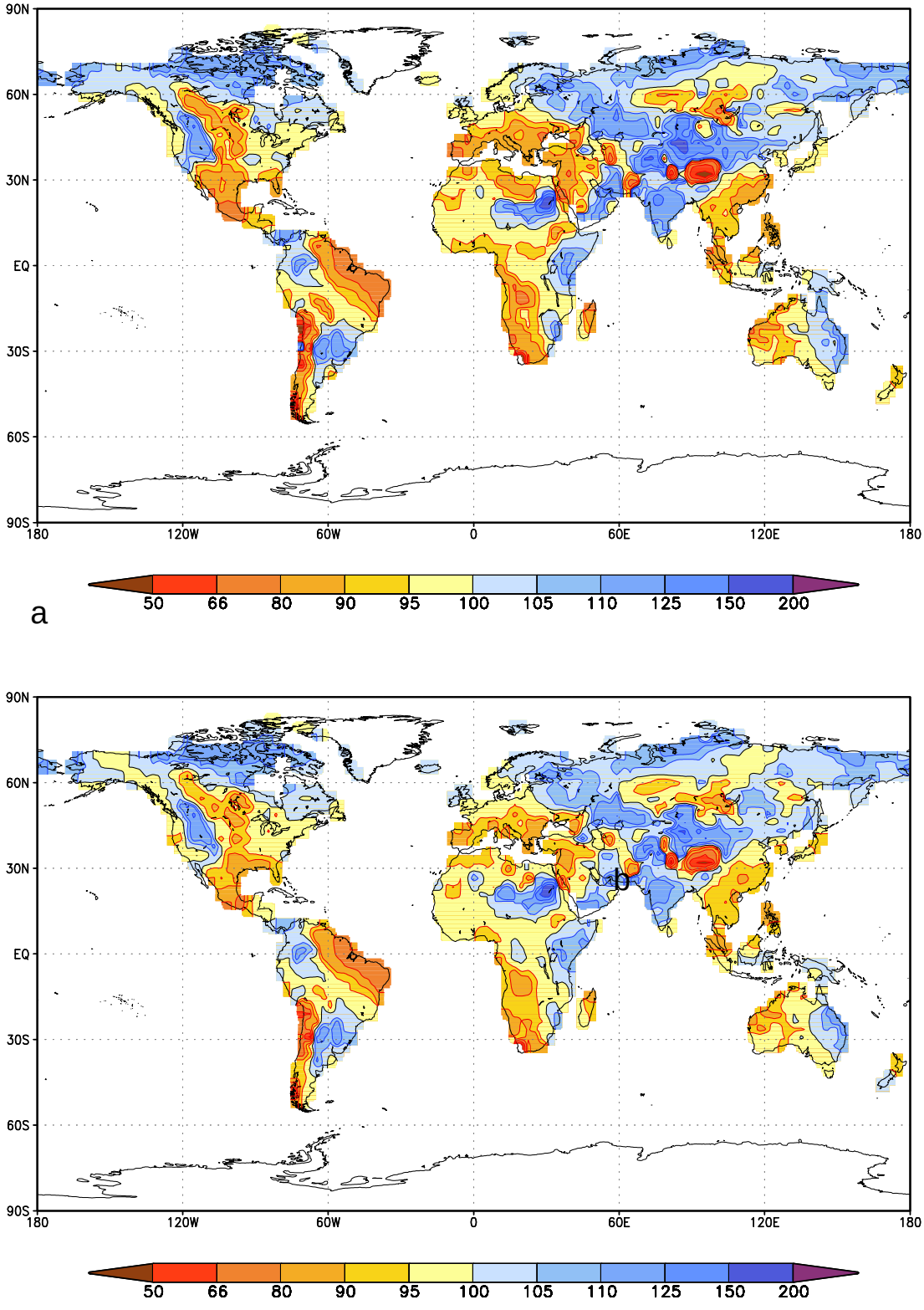

Fig. 7: As Fig. 4, for soil moisture [cm water column].

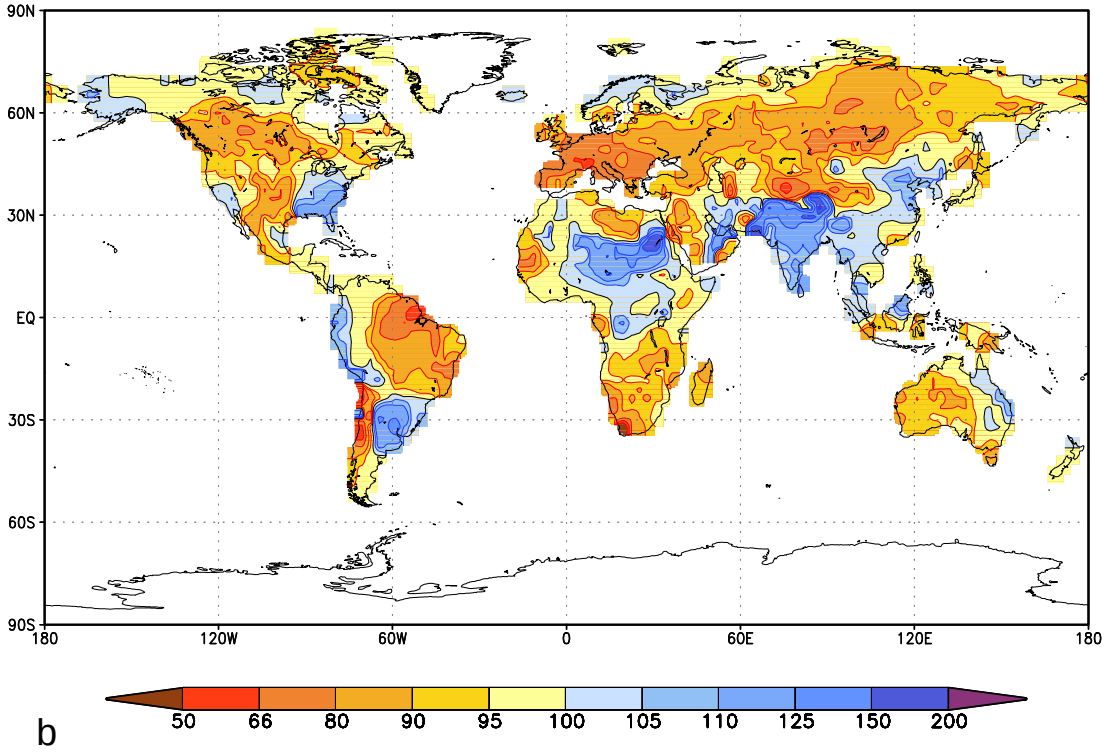

b

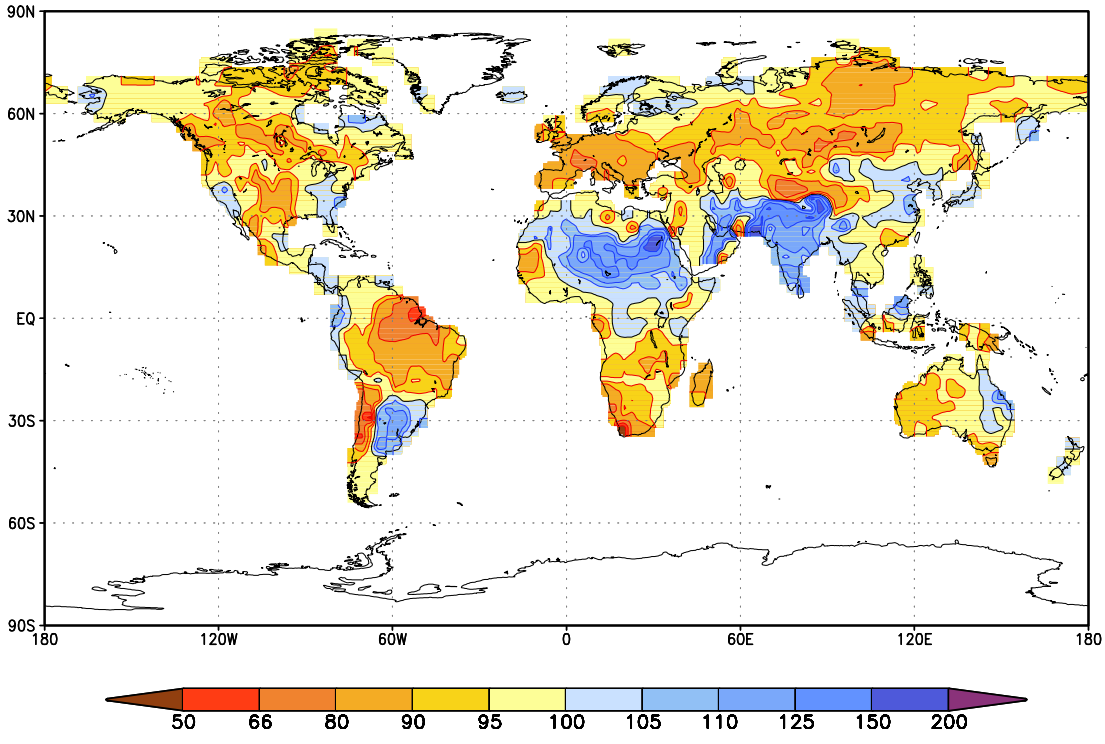

Fig. 7 (continued)

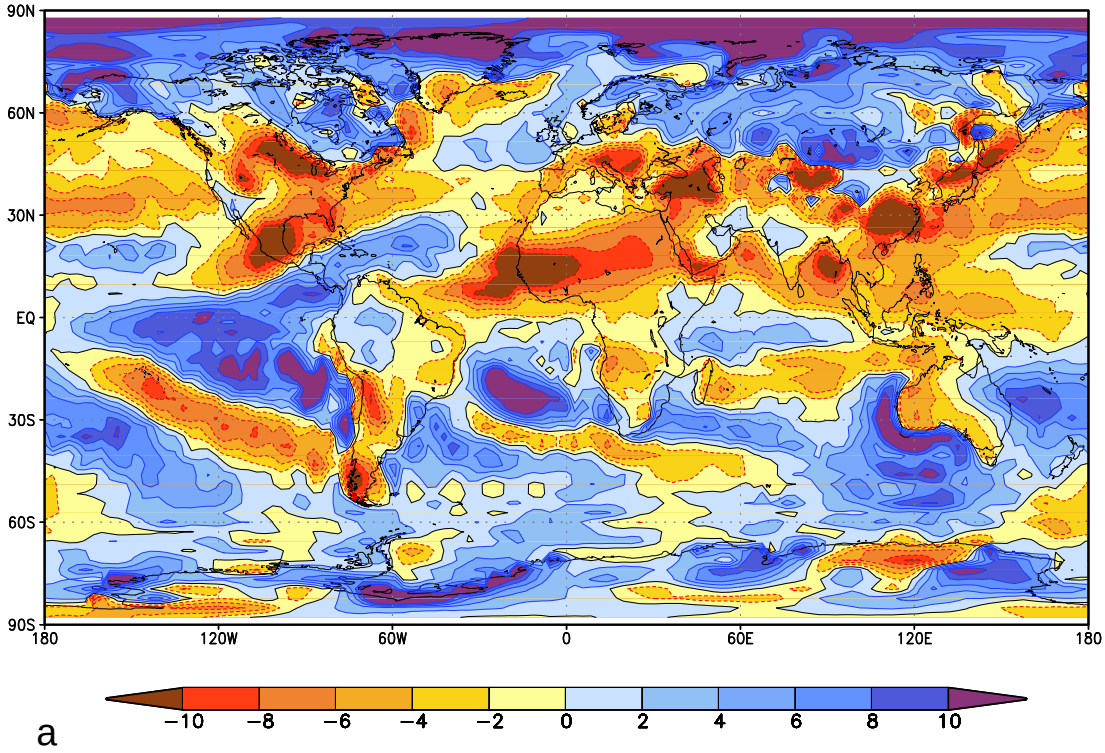

a

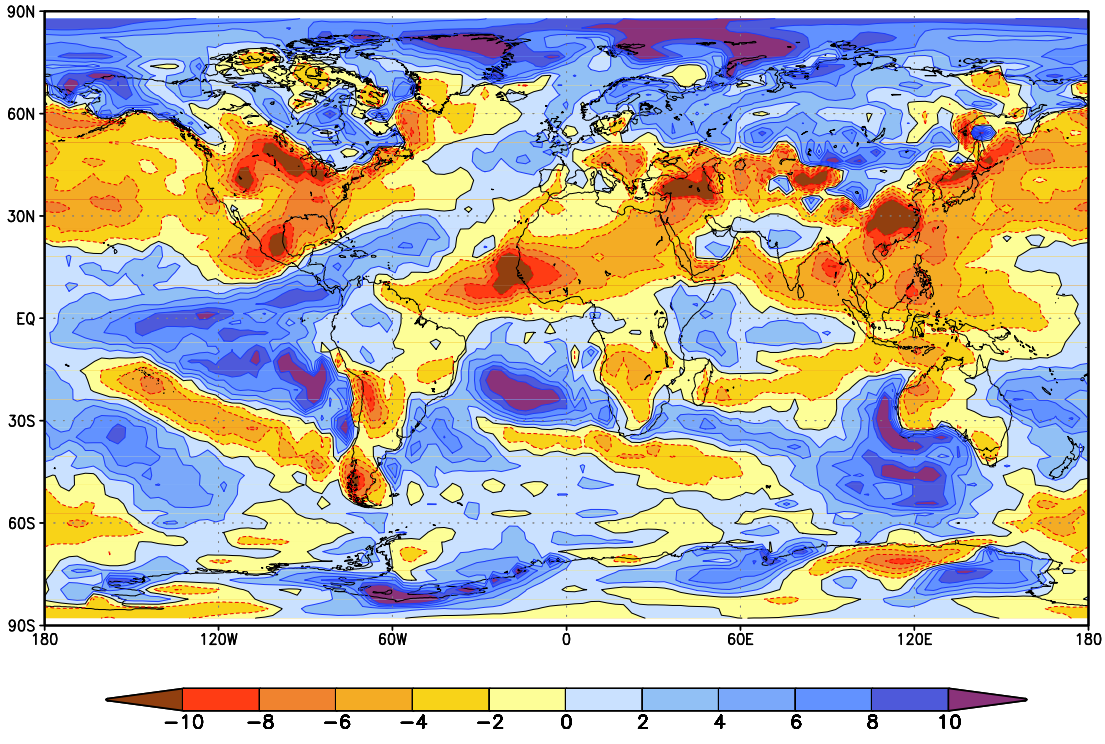

Fig. 8: As Fig. 4, for cloud cover [%].

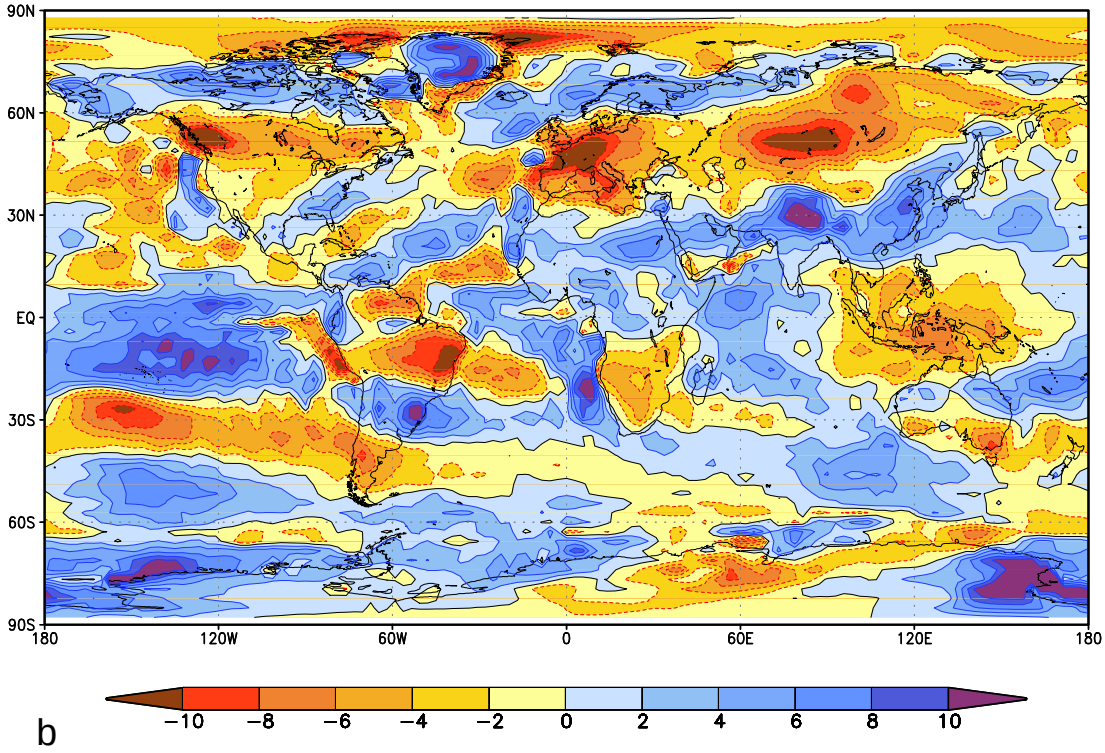

b

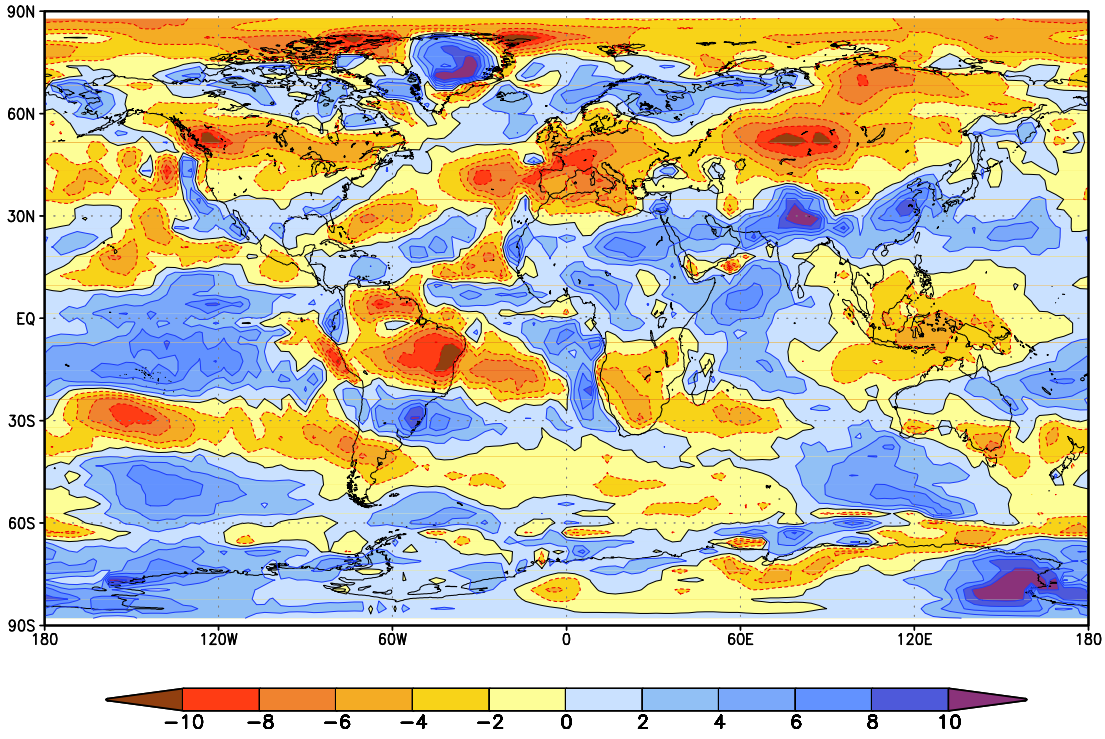

Fig. 8 (continued)

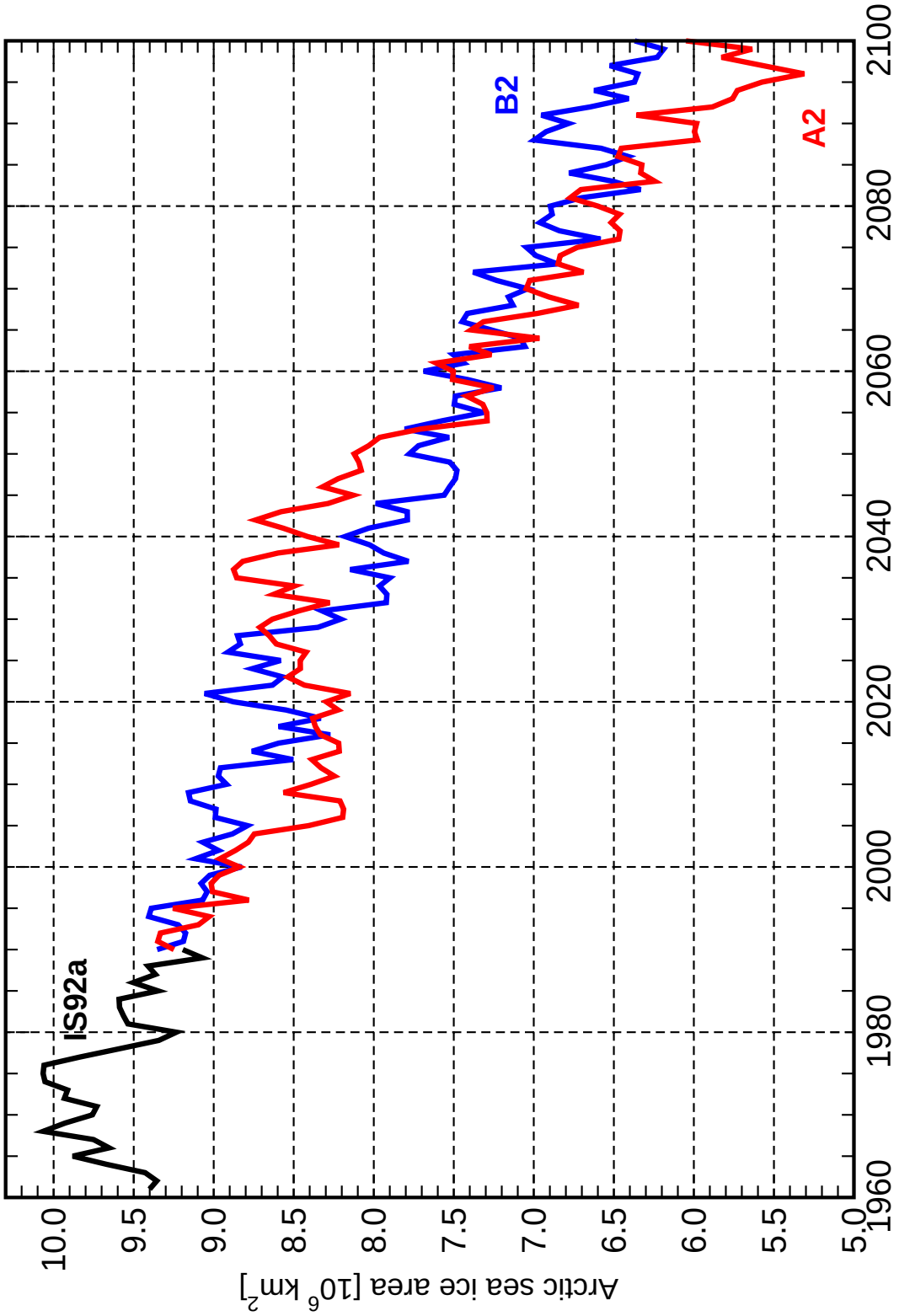

Fig. 9: Temporal evolution of Arctic sea-ice cover [10^6 km^2] for the simulations GSDIO (Roeckner et al., 1999), A2 and B2.

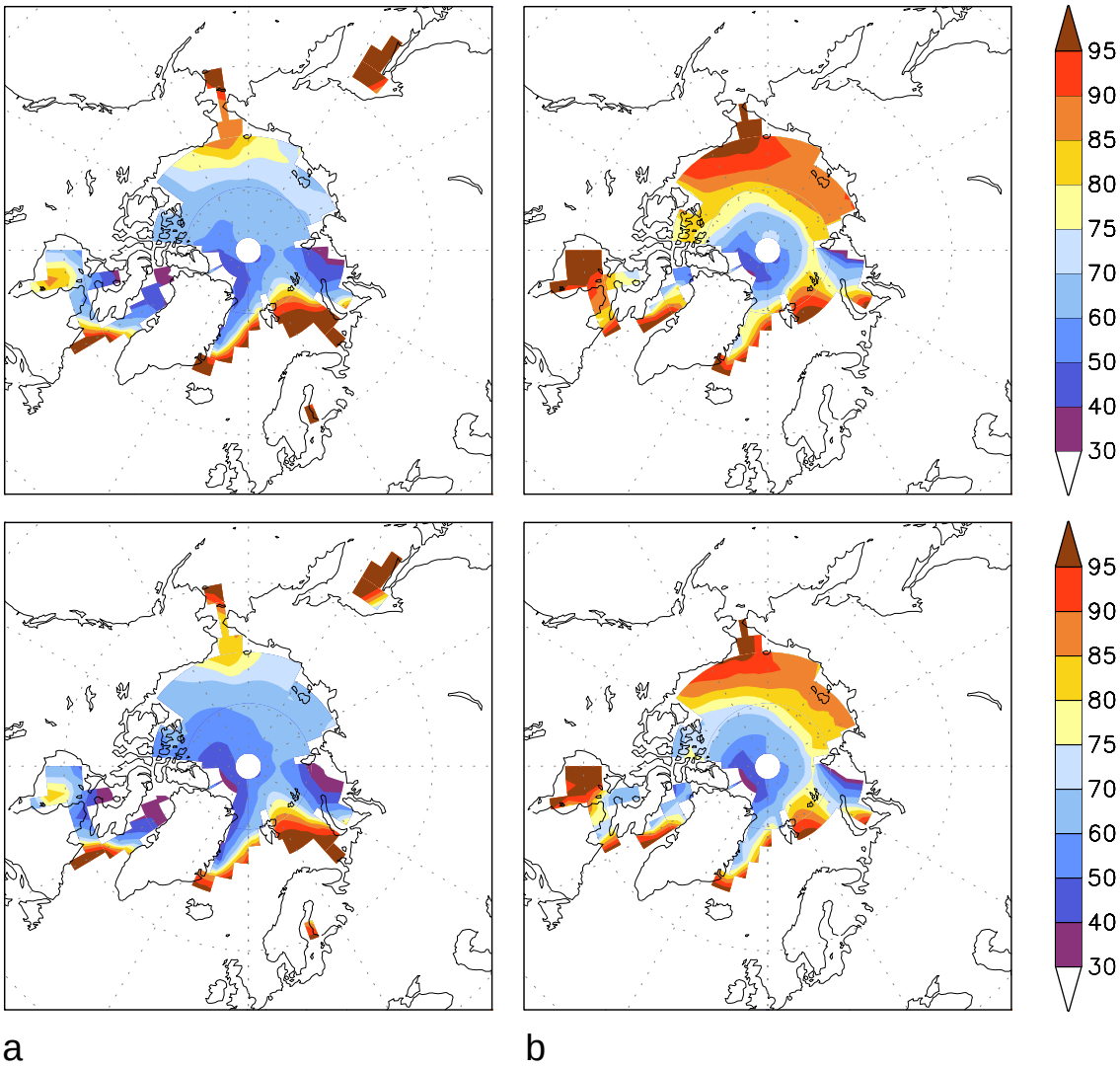

Fig. 10: Percentage reduction in sea-ice volume (a) in DJF, (b) in JJA for the period 2071-2100 compared to the period 1961-1990. Top: scenario A2, bottom: scenario B2.

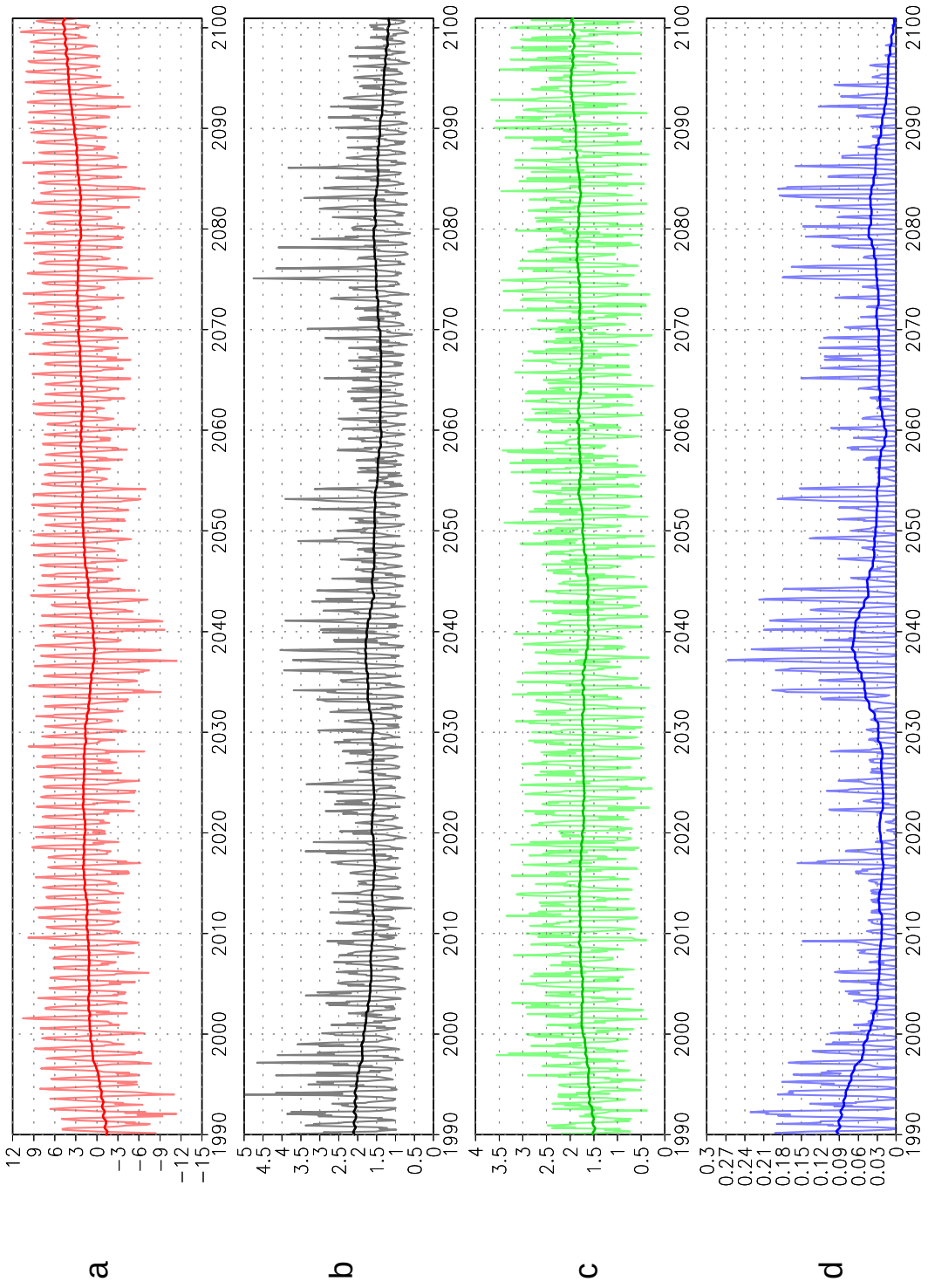

Fig. 11: Temporal evolution of the monthly means of (a) near-surface temperature [°C] , (b) sea level pressure [hPa], (c) precipitation [mm day^{-1}] and (d) sea-ice cover [10^6 km^2] in the Barents Sea region (70°–80°N, 30°–50°E) in Scenario A2.

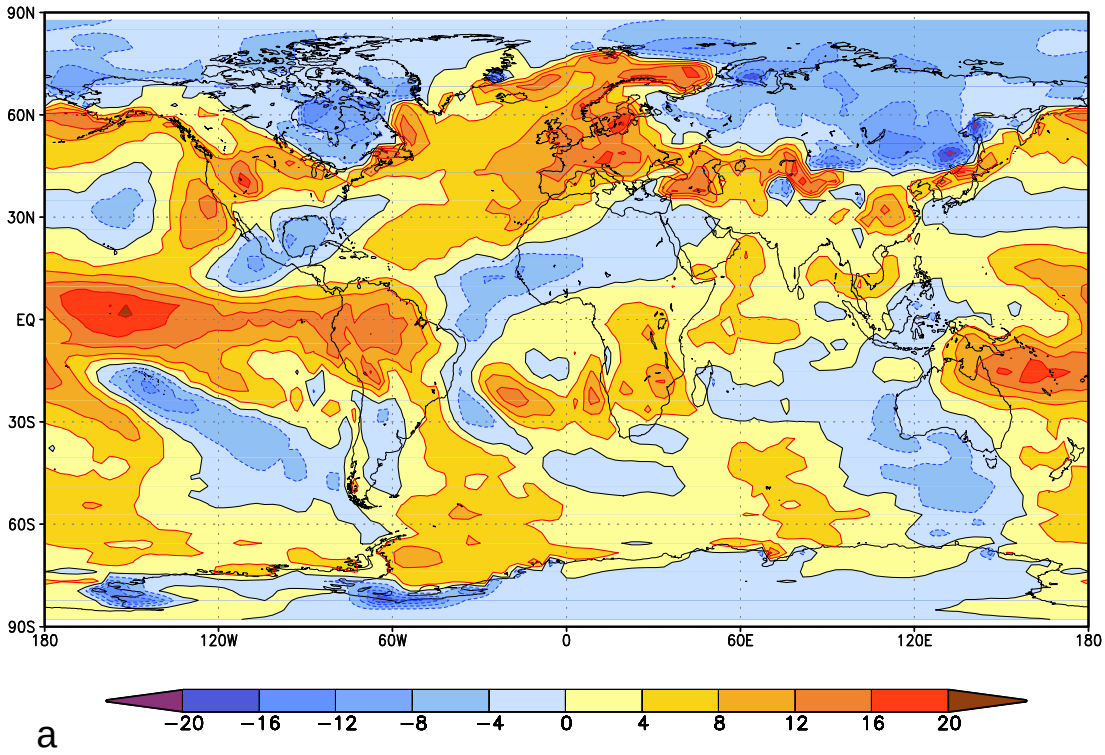

a

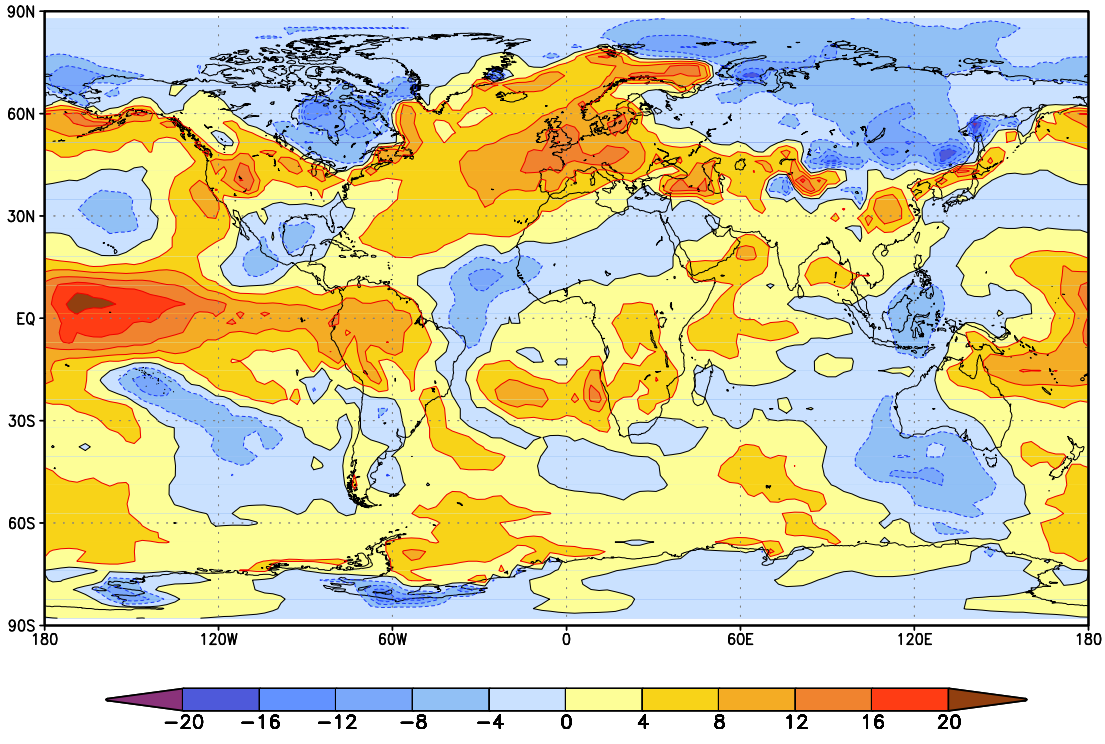

Fig. 12: As Fig. 4, for atmospheric (=top of atmosphere minus surface) longwave cloud forcing [W m^{-2}].

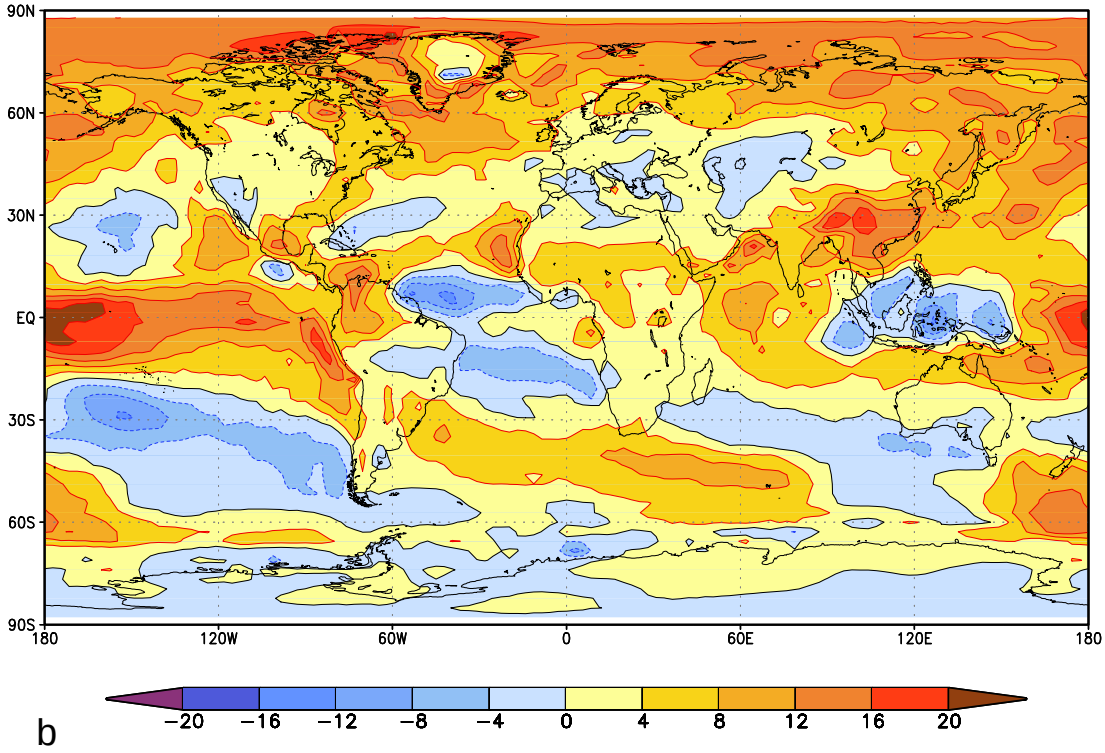

b

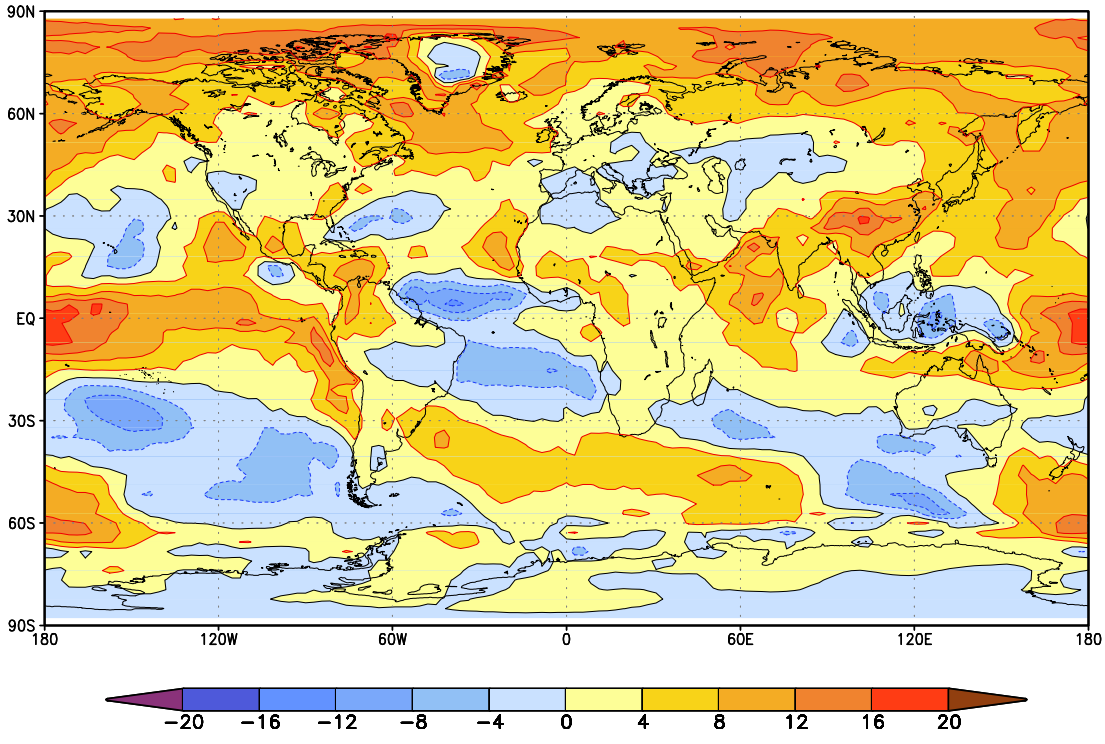

Fig. 12 (continued)

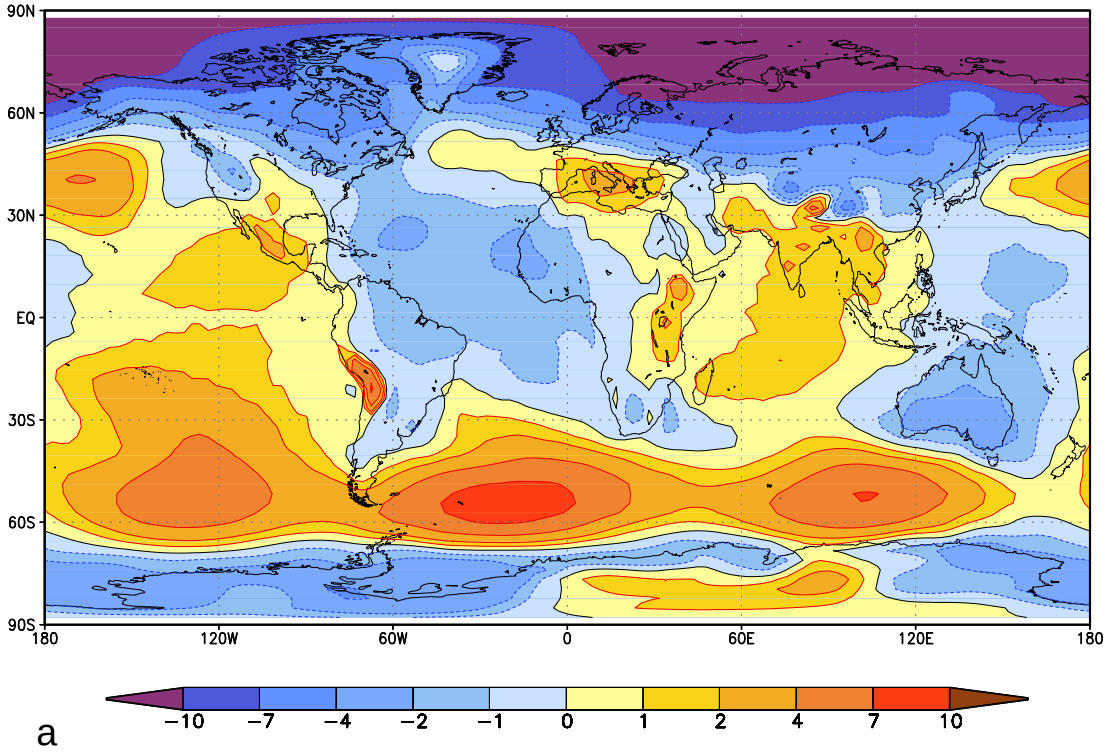

a

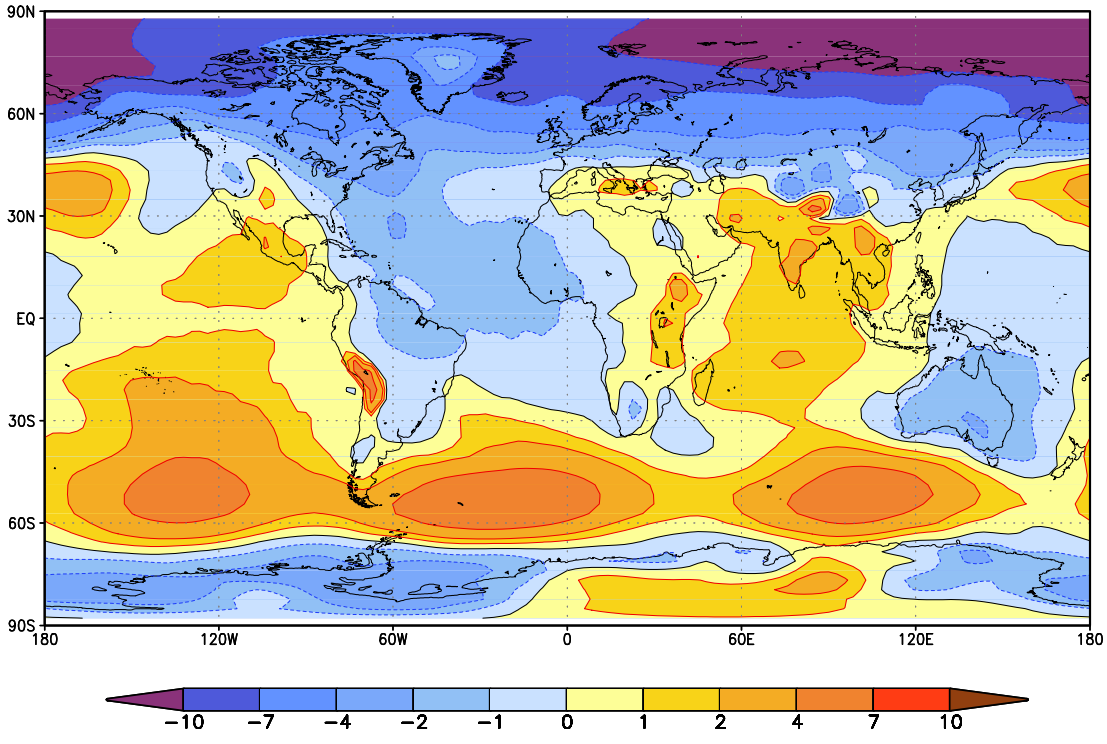

Fig. 13: As Fig. 4, for sea level pressure [hPa].

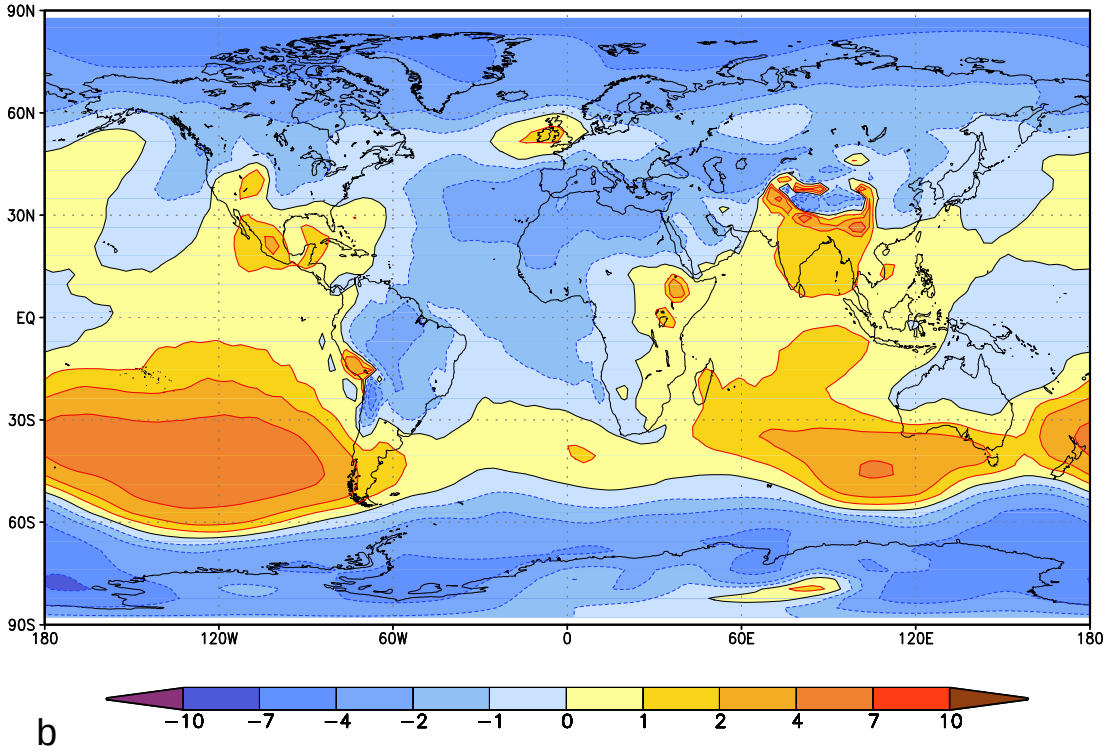

b

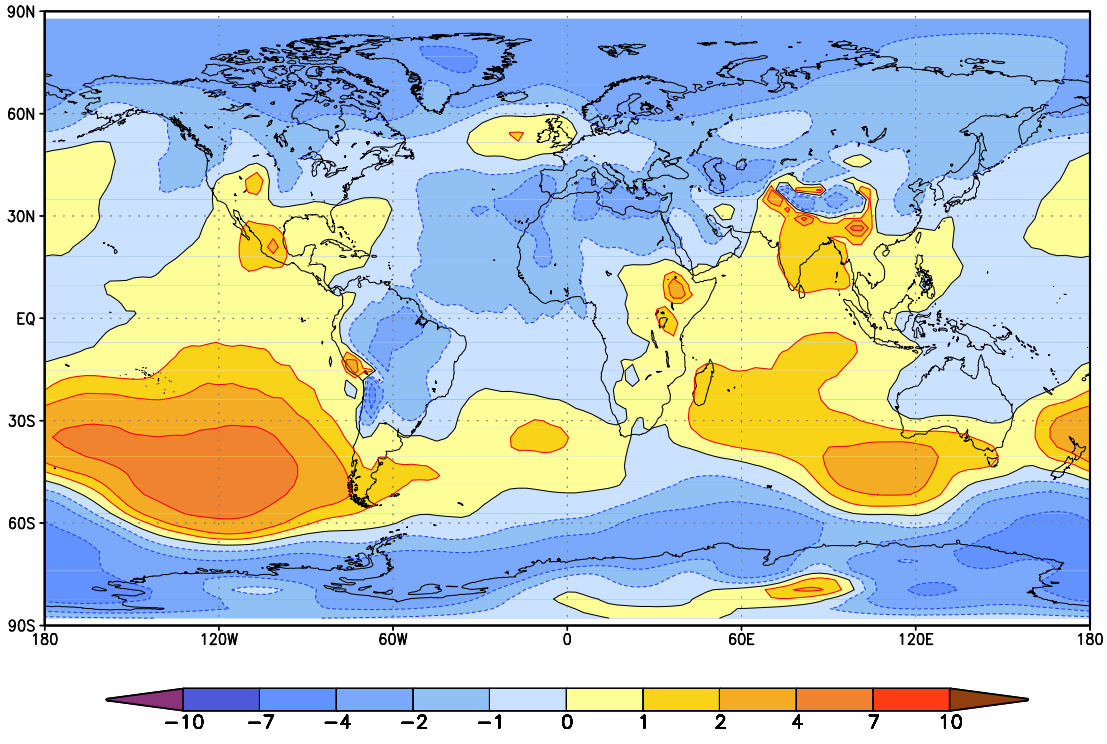

Fig. 13 (continued)

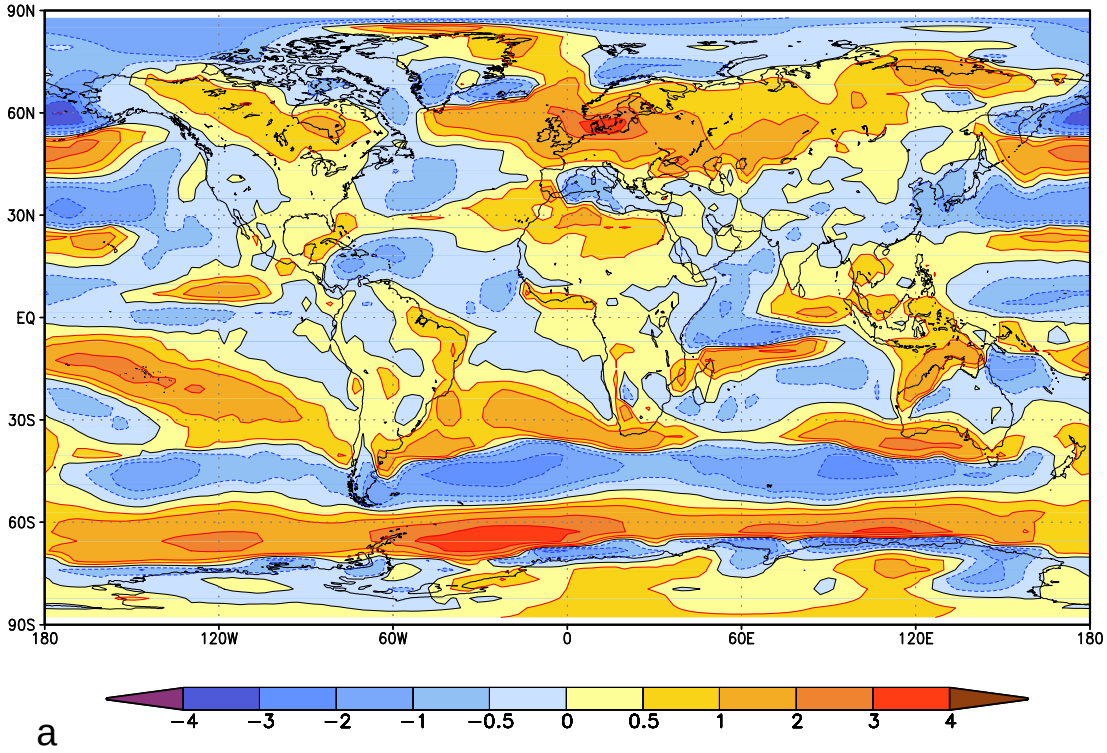

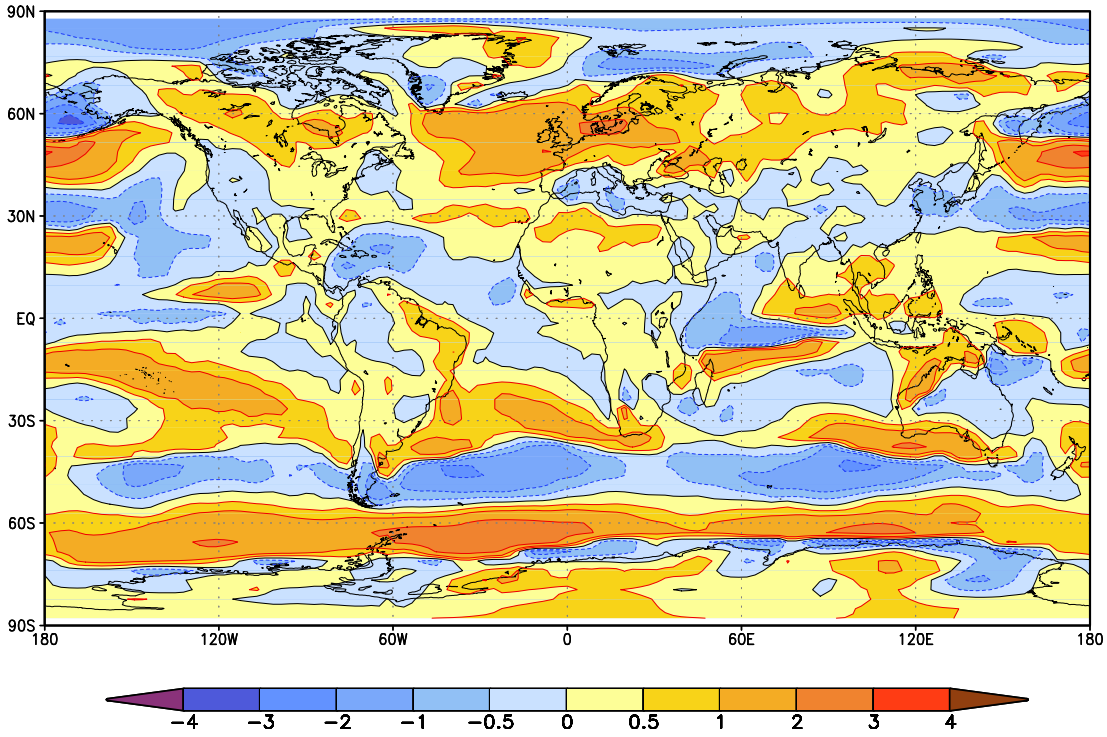

Fig. 14: As Fig. 4, for 10 m wind speed [m s^{-1}].

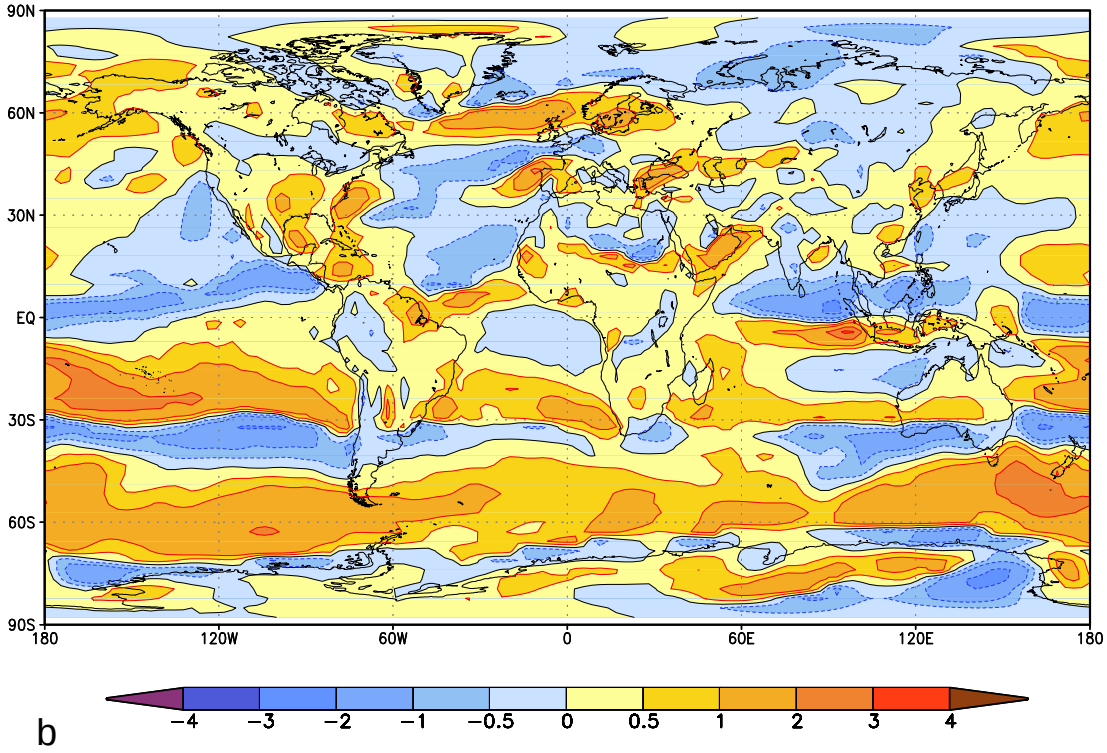

b

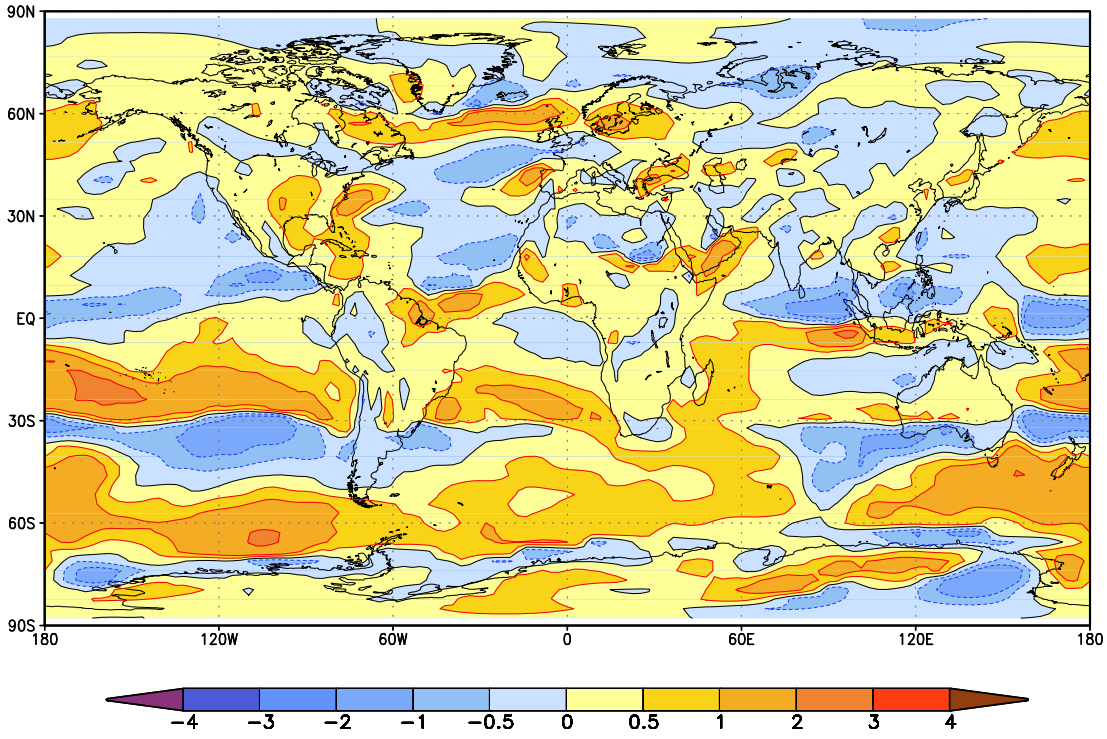

Fig. 14 (continued)

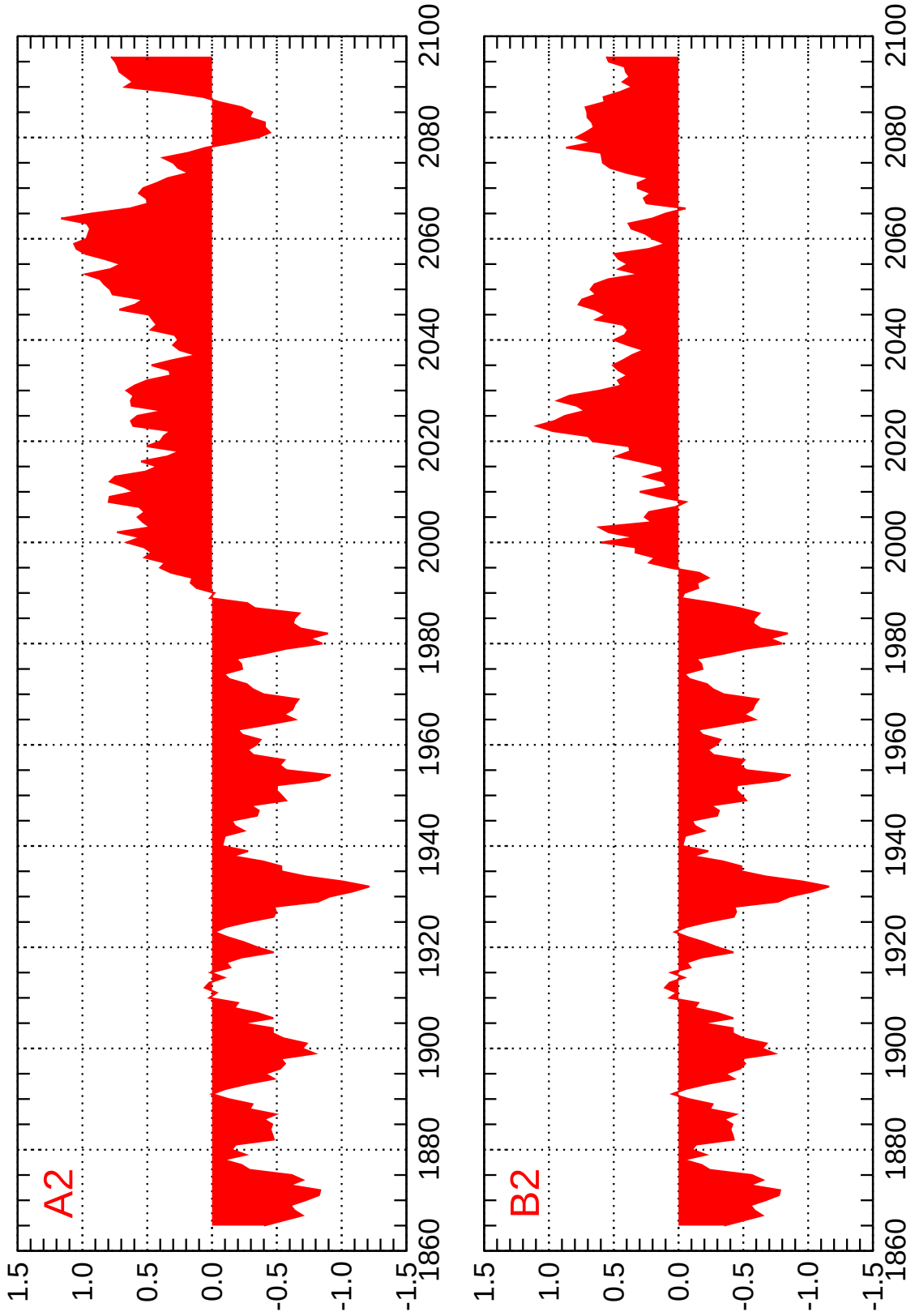

Fig. 15: Time series of the NAO index, calculated from the normalized DJF pressure difference Gibraltar (36°N, 6°W) minus Stykkisholmur/Iceland (65°N, 23°W). A nine year running mean has been applied.

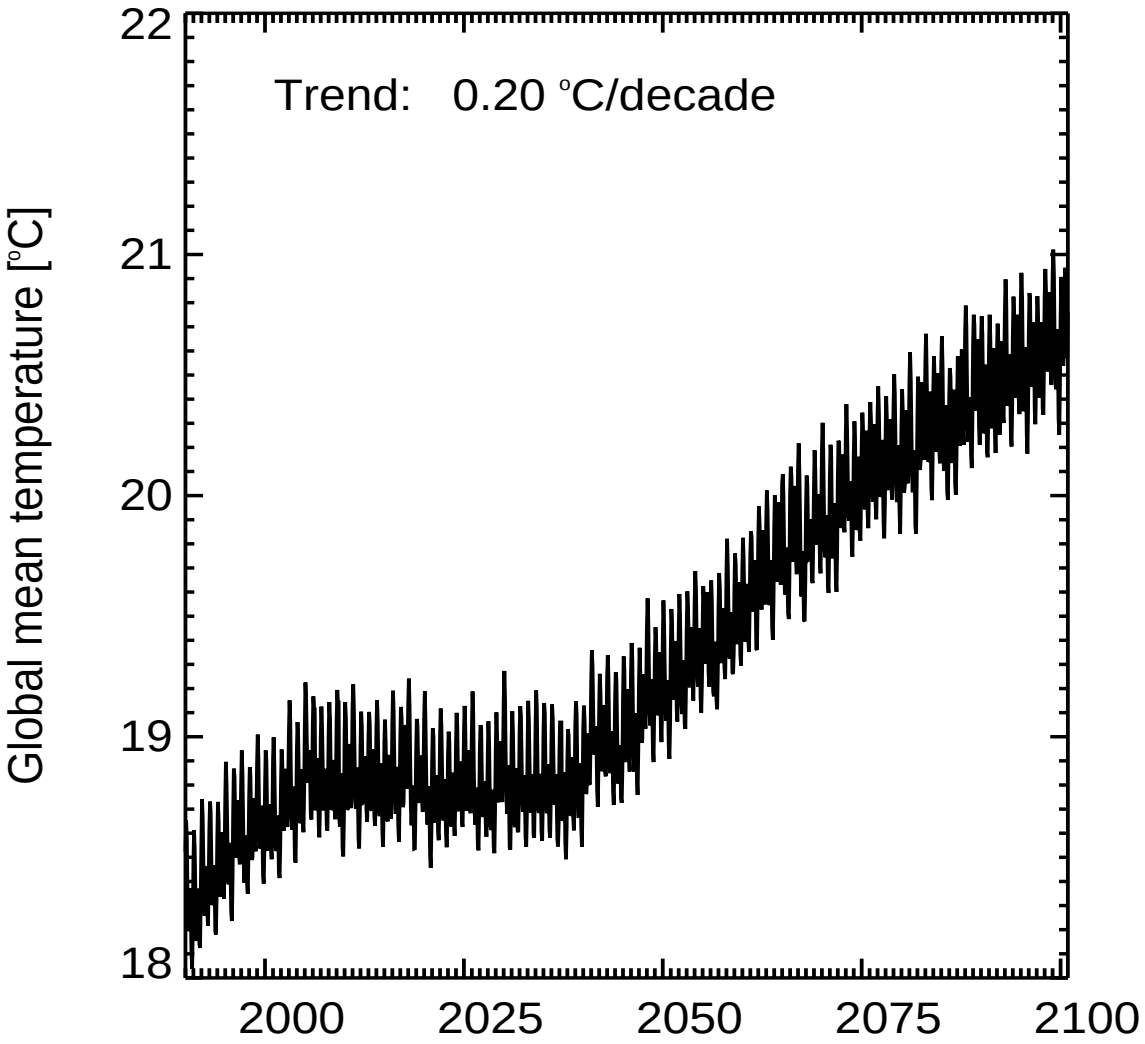

Fig. 16: Evolution of global average of the monthly mean SST [°C] for scenario A2.

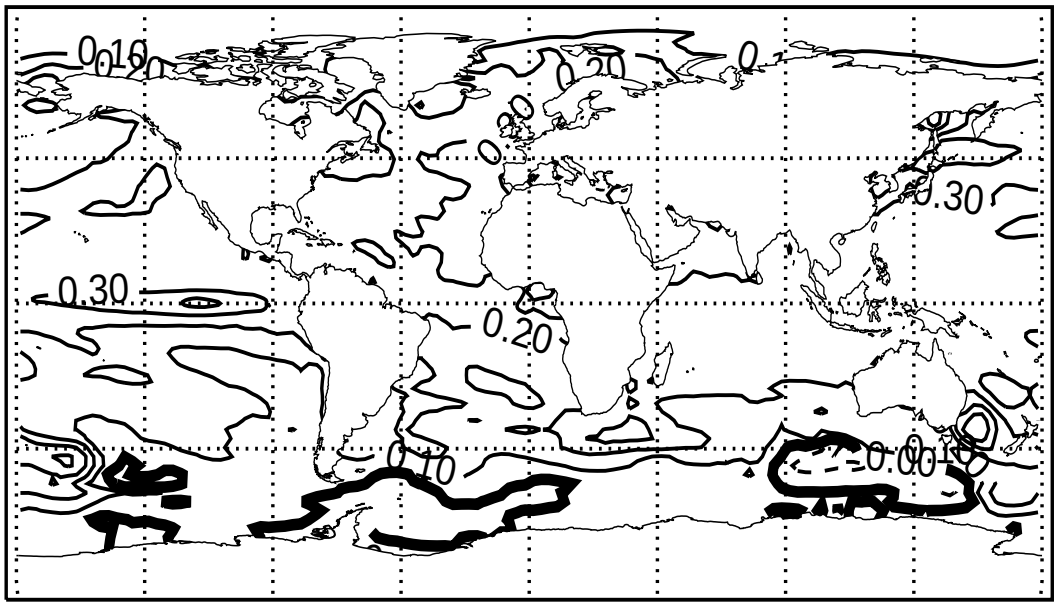

Fig. 17: Geographical distribution of the average trend in SST over the period 1990-2090 for scenario A2. Contour interval: 0.1 K/decade.

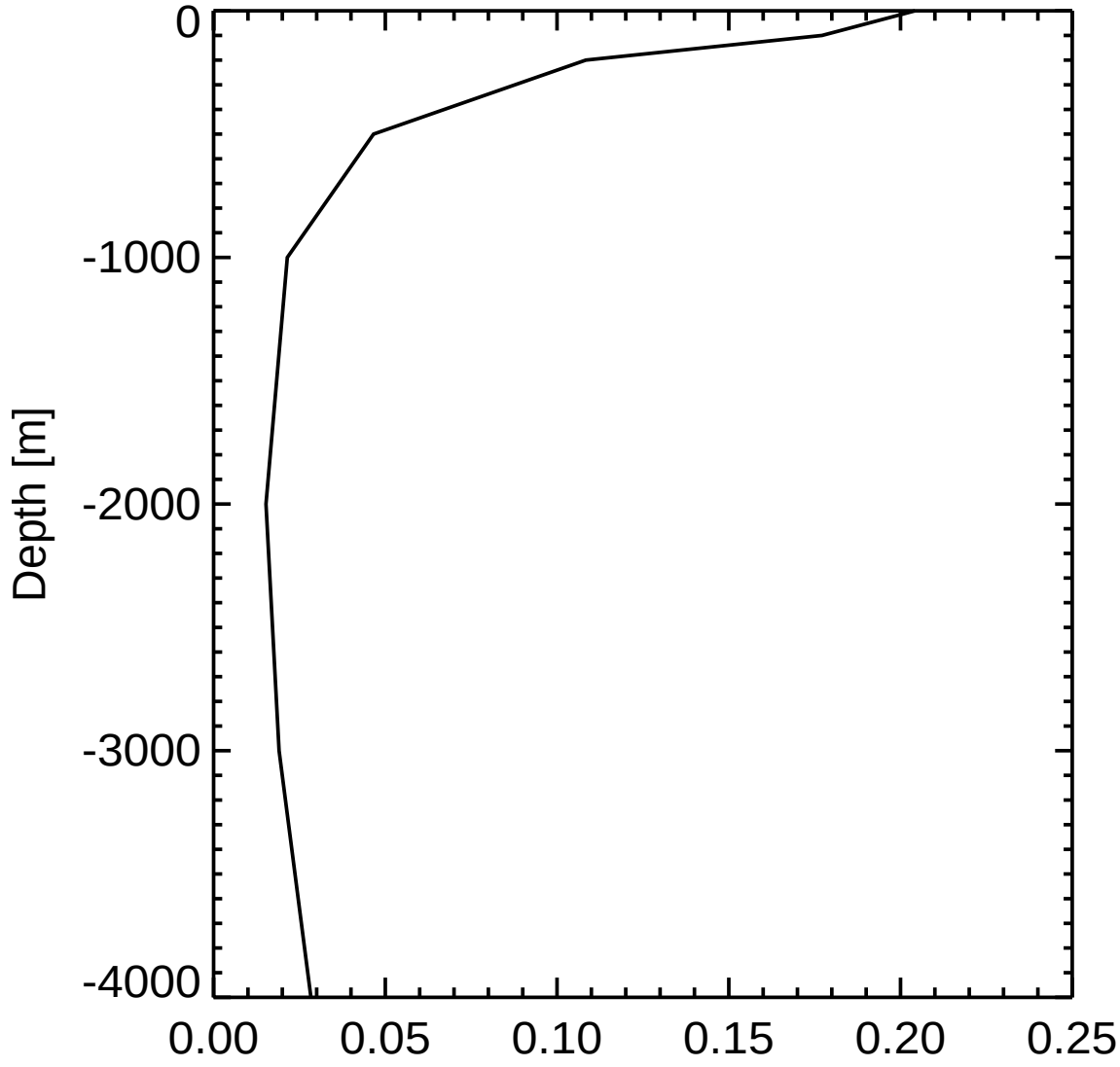

Fig. 18: Vertical cross section of globally averaged monthly mean temperature trends [K/decade] for scenario A2.

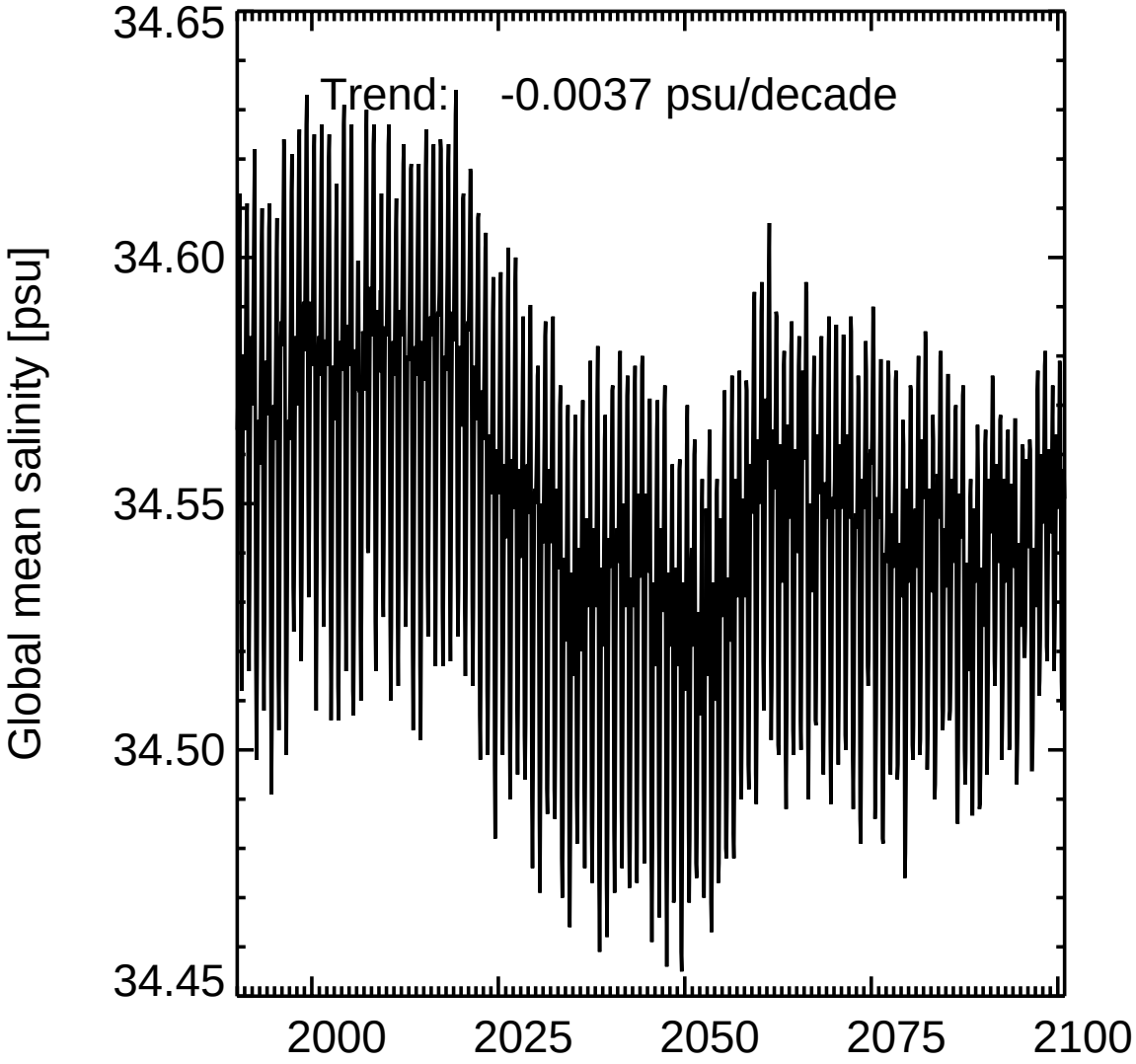

Fig. 19: Evolution of global average of the monthly mean SSS [psu] for scenario A2.

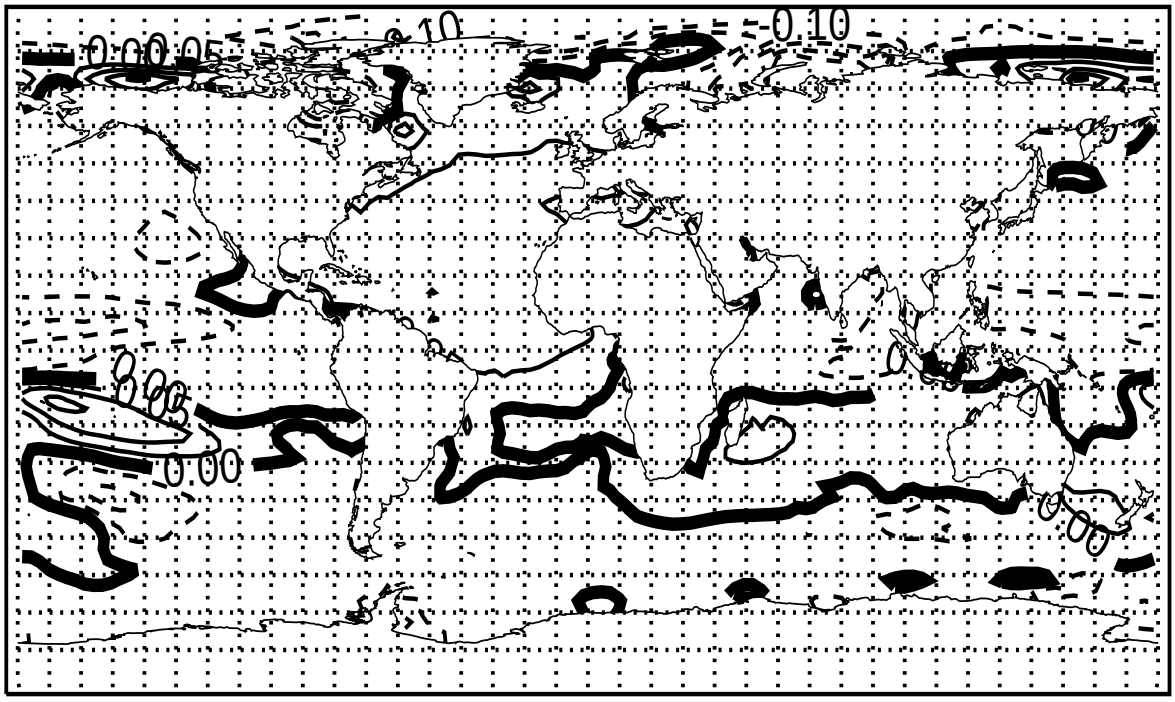

Fig. 20: Geographical distribution of the average trend in SSS over the period 1990-2090 for scenario A2. Contour interval: 0.1 psu/decade.

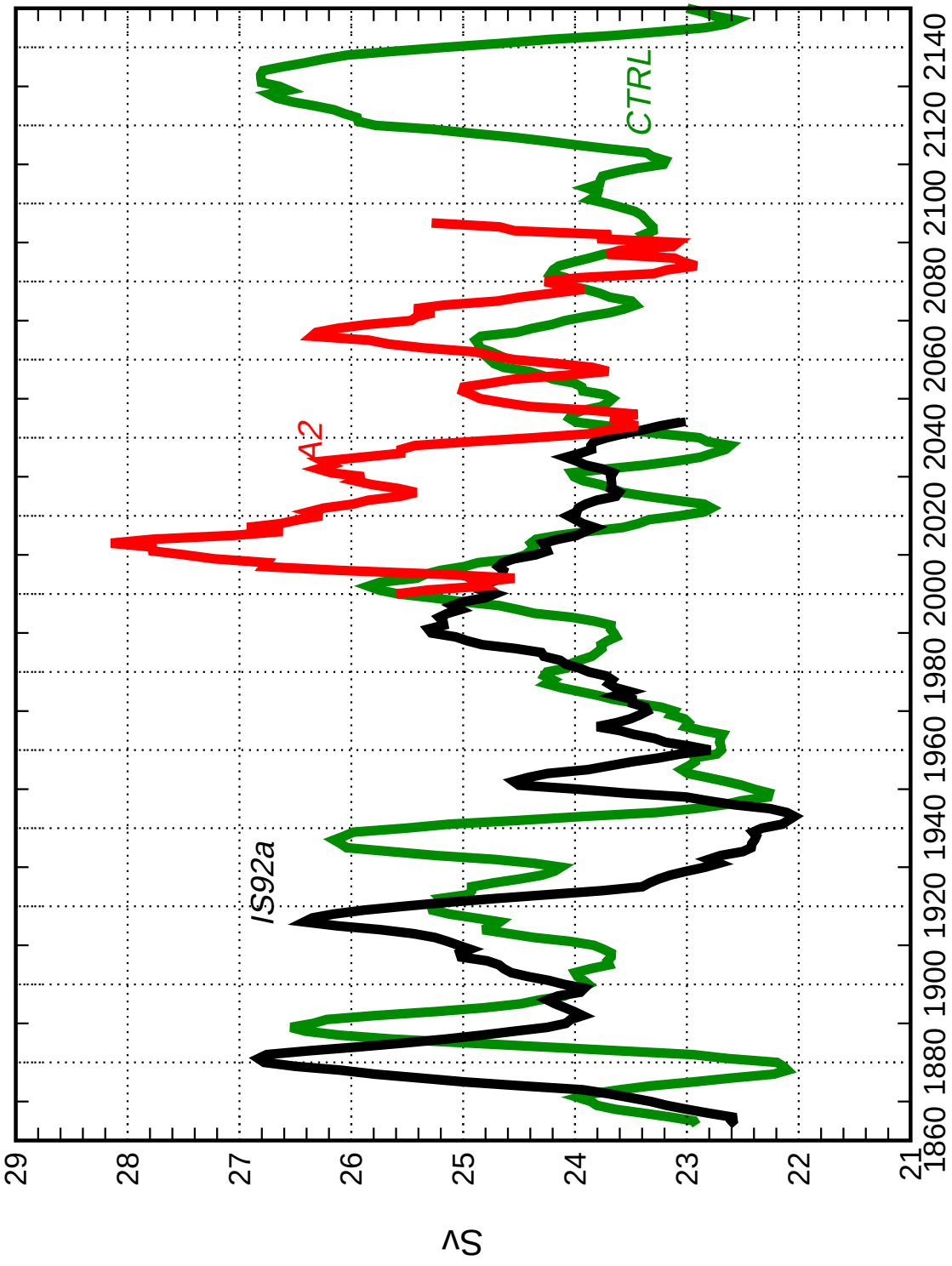

Fig. 21: Time series of the Atlantic meridional overturning circulation [Sv], defined as the maximum value of the transport stream function over the area 30°S to 90°N for the control simulation and the scenarios IS92a (GSDIO experiment of Roeckner et al., 1999) and A2.

The Danish Climate Centre

The Danish Climate Centre was established at the Danish Meteorological Institute in 1998. The main objective is to project climate into the 21st century for studies of impacts of climate change on various sectors and ecosystems in Denmark, Greenland and the Faroes.

The Climate Centre activities include development of new and improved methods for satellite based climate monitoring, studies of climate processes (including sun-climate relations, greenhouse effect, the role of ozone, and air/sea/sea-ice interactions), development of global and regional climate models, seasonal prediction, and preparation of global and regional climate scenarios for impact studies.

The Danish Climate Centre is organised with a secretariat in the Research and Development Department, and it is co-ordinated by the Director of the Department. It has activities also in the Weather Service Department and the Observation Department, and it is supported by the Data Processing Department.

The Danish Climate Centre has established the Danish Climate Forum for researchers in climate and climate related issues and for others having an interest in the Danish Climate Centre activities. The Centre issues a quarterly newsletter KlimaNyt (in Danish).

DMI has been doing climate monitoring and research since its foundation in 1872, and establishment of the Danish Climate Centre has strengthened both the climate research at DMI and the national and international research collaboration.

Previous reports from the Danish Climate Centre:

- Dansk Klimaforum 29.-30. april 1998. (Opening of Danish Climate Centre and abstracts and reports from Danish Climate Forum workshop). *Climate Centre Report 98-1* (in Danish).
- Danish Climate Day 1999. *Climate Centre Report 99-1*.
- Dansk Klimaforum 12. april 1999. Workshop: Klimatisk variabilitet i Nordatlanten på tidsskalaer fra årtier til århundreder. *Climate Centre Report 99-2* (in Danish).
- Luftfart og den globale atmosfære, Danmarks Meteorologiske Instituts oversættelse af IPPC's særrapport "Aviation and the Global Atmosphere, Summary for Policymakers". *Climate Centre Report 99-3* (in Danish).
- Forskning og Samarbejde 1998-1999. *Climate Centre Report 00-1* (in Danish).
- Drivhuseffekten og regionale klimaændringer. *Climate Centre Report 00-2* (in Danish).
- Emissionsscenarier, Danmarks Meteorologiske Instituts oversættelse af IPPC's særrapport "Emissions Scenarios, Summary for Policymakers". *Climate Centre Report 00-3* (in Danish).
- Metoder mødes: Geofysik og emner af samfundsmæssig interesse. Dansk Klimaforums Workshop 15.-16. maj 2000. *Climate Centre Report 00-4* (in Danish).
- A time-slice experiment with the ECHAM4 A-GCM at high resolution: The simulation of tropical storms for the present-day and of their change for the future climate. *Climate Centre Report 00-5*.
- The climate of the 21st century: Transient simulations with a coupled atmosphere-ocean general circulation model. *Climate Centre Report 00-6*.
- Changes in the storm climate in the North Atlantic / European region as simulated by GCM time-slice experiments at high resolution. *Climate Centre Report 01-1*.
- Klimadag 26 april 2001, Klimaændringer og deres virkninger. *Climate Centre Report 01-2* (in Danish).
- Synthesis of the STOWASUS-2100 project: Regional storm, wave and surge scenarios for the 2100 century. *Climate Centre Report 01-3*.
- Danmark, Færøerne og Grønlands Klima. DMIs afrapportering til FNs Klimakonvention UNFCCC. *Climate Centre Report 01-4* (in Danish).
- Danmarks vejr og klima i det 20. århundrede. *Climate Centre Report 01-5* (in Danish).
- Using the nudging technique to estimate climate model forcing residuals. A contribution to the ACE Scientific Support Study. *Climate Centre Report 01-6*.
- Detection of the Pinatubo volcanic heating signal in the lower stratosphere based on nudging assimilation and analysis increments. *Climate Centre Report 01-7*.
- PRUDENCE kick-off meeting, Snekkersten December 3-5, 2001. *Climate Centre Report 01-8*.
- Klimaændringer 2001 - Den videnskabelige baggrund. En rapport fra IPCCs arbejdsgruppe I, Resume for beslutningstagere. DMIs oversættelse af Climate Change 2001 - The Scientific Basis, A report of Working Group I of the International Panel on Climate Change, Summary for policymakers. *Climate Centre Report 01-9* (in Danish).